

Abstract

SMITH II, BARRETT LEE. The Interaction of Moisture Fluxes and Orographic Precipitation over Northern California Associated with a Landfalling Atmospheric River. (Under the direction of Sandra E. Yuter.)

Atmospheric rivers emanating from the tropics are responsible for the majority of the meridional transport of water vapor in the Northern Hemisphere, and have also been linked to episodes of heavy orographic precipitation along the mountains of the U.S West Coast. As moist air flow impinges on mountain ranges, orographic lifting converts water vapor to precipitation and can greatly reduce the moisture content of the airmass. The nearly along-coast parallel orientation of the Coastal and Sierra Nevada Ranges in Northern California, and the proximity of the Petaluma Gap to the south along the coast yield a geography, where moisture may enter the Sacramento Valley from multiple locations, complicating the quantification of airmass transformation over the region. Limitations of surface and satellite observing networks further complicate these calculations. In this study, the Weather Research and Forecasting Model (WRF) Version 2.2 is used to investigate the moisture flux and three-dimensional airmass transformation over northern California associated with the 29-31 December 2005 atmospheric river. Moisture flux analysis of the storm reveals that moisture enters the Sacramento Valley by both flowing over and around the Coastal Range. A large portion of the flow-over moisture is converted to precipitation along the windward slopes. Flow-around moisture enters through the Petaluma Gap, and then a significant portion is deflected northward by the strong barrier jet associated with the Sierra Nevada range. Moisture convergence and orographic lifting enhance precipitation along the slopes of the Sierra Nevada and Siskiyou Ranges. A drying ratio, or moisture reduction, of nearly 55%

is found for the entire mountain complex, with 30% and 25% for the Coastal and Sierra Nevada Ranges, respectively. In a model sensitivity test where the Coastal Range is removed, the amount of moisture reaching the Sierras is only slightly increased compared to when the Coastal Range is present. When all terrain is removed, there is little reduction of moisture flux by the ocean/coast boundary, and the atmospheric river is able to penetrate deep into the western U.S.

The Interaction of Moisture Fluxes and Orographic Precipitation
Over Northern California Associated with a Landfalling
Atmospheric River

by

Barrett Lee Smith, II

A thesis submitted to the Graduate Faculty of
North Carolina State University
in partial fulfillment of the
requirements for the degree of
Master of Science

Marine, Earth, and Atmospheric Sciences

Raleigh, North Carolina

2007

APPROVED BY:

Sandra Yuter

Chair of Advisory Committee

Gary Lackmann

Matthew Parker

Dedication

My thesis is dedicated to my grandmothers. To Audrey Byrd, whose dream it would have been to see her grandchildren graduate college, for her endless love and generosity, and to Hazel Smith, for being the perfect example of strength and dedication.

Acknowledgements

First and foremost, thanks to my family for their love and support, and to my boys for just being THEM AGAIN. To Shannon for standing by my side and the countless words of encouragement. Special thanks to Sandra Yuter for taking me on as an advisee and supporting me the last six months of graduate school. Thanks to Gary Lackmann and Matt Parker for sitting on my committee and providing input. Also to David Kingsmill and Paul Neiman for their input on atmospheric rivers, to Ron Smith for conversations on drying ratios, to Brian Colle and Scott Braun for modeling advice, and to Anantha Aiyyer for discussions on water vapor budgets. Thanks to Rob Fovell for model terrain removal code.

Many thanks to the members of the Mesolab; Heather Reeves, Christine Huang, Allison Hoggarth, Major David Vollmer, Mike Kiefer, Zach Brown, Chad Ringley, Steve Harville, and Kristian Horvath for help on so many things, inside and outside of the lab. To Morgan Silverman for daily walks and Paul Suffern for lunch trips to K&W. Also, to the members of the Forecasting Lab, the Cloud and Precipitation Processes and Patterns Group, and Convective Storms Group. Many, many thanks to Ben Baranowski for helping me get the water vapor budget started. Thanks also to Connie Hockaday and everyone in the Jordan Hall main offices. To Jack Neely and the PAMS Linux Cluster at N.C.S.U. for providing computational space for numerical simulations, the Earth System Research Laboratory Global Systems Division, and the Hydrometeorological Testbed Program for providing necessary data.

Thanks to everyone at the National Weather Service for being patient, helping with my work schedule, and allowing me to spend quiet nights working on my thesis. And speaking

of quiet nights... somehow I have to thank *the Drought of 2007* for giving me those quiet weather nights to work.

Finally, to all of those above and anyone else I failed to mention who crossed my path along the way... each of you has contributed to this thesis and my life in one way or another, and for that I will forever be grateful.

Table of Contents

List of Figures	viii
List of Tables	xii
1 Introduction	1
2 Background	4
2.1 Field projects.....	4
2.2 The low-level jet	5
2.3 Atmospheric rivers.....	6
2.4 Airmass transformation.....	7
2.4.1 Blocked vs. unblocked flow.....	7
2.4.2 Drying ratios	8
3 Data	10
4 Methodology	12
4.1 Regional model design.....	12
4.2 Moisture budget	13
4.2.1 Integrated water vapor	14
4.2.2 Horizontal moisture flux	15
4.2.3 Regional scale budget	15
4.2.4 Small scale budgets.....	18
5 29-31 December 2005 Case Description	19
6 Model Verification	21
6.1 Synoptic flow and atmospheric river	21
6.2 The barrier jet.....	22
6.3 Precipitation	22
6.4 Regional Scale Budget.....	23
7 Results	24
7.1 Positive-definite moisture transport.....	24
7.2 CTRL	25
7.2.1 Moisture flux analysis.....	25

7.2.2 Small scale budget	27
7.3 NOCR	29
7.4 NOTER	30
7.5 IWV Totals.....	32
7.6 Moisture flux totals.....	33
7.7 Precipitation totals	34
8 Conclusions	36
9 Future Work.....	39
Bibliography	74

List of Figures

Figure 1	California terrain elevation with and overlay of (a) significant geographical locations referenced in the text and (b) GPS-IPW locations and the Oakland sounding site.....	40
Figure 2	Average annual rainfall for northern California from 1961-1990. (Source: Oregon Climate Service).....	41
Figure 3	Highest river flood stage observed from December 24, 2005 to January 7, 2006. Source: California Nevada River Forecast Center.....	42
Figure 4	Composite SSM/I IWV (left) and NCEP reanalysis IWV and fronts (right) of winter atmospheric river cases making landfall on California coast (from Neiman et al. 2007). Units of IWV in cm	43
Figure 5	Fifth Generation Pennsylvania State University-UCAR Mesoscale Model (MM5) low-level (their σ level 0.95) winds (arrows in $m\ s^{-1}$) and θ_e (shaded in K) from Galewsky and Sobel (2005) for the New Year's Day flood of 1996 for (a) 31 Dec. 1996, and (b) 1 Jan. 1997; (c) Observed precipitation (mm) from 00 UTC 31 Dec., 1996 – 00 UTC 4 Jan., 1997.	44
Figure 6	WRF model domain set up for 27 km outer and 9 km inner domains, and the large scale water vapor budget domain within the inner model domain.	45
Figure 7	WRF model terrain elevation (shaded in m) for (a) CTRL, (b) NOCR, and (c) NOTER runs (each labeled), and cross section reference lines labeled Y and Z.	46
Figure 8	WRF model terrain (shaded) with (a) the assignment of positive and negative flux values used in the moisture flux analysis of box sides (the same convention applies to each box side), and (b) layout of small scale moisture budget boxes with sides labeled A-P and boxes labeled 1-5. Note: sign conventions here are not the same as those used in the moisture budget.	47
Figure 9	NARR 500 mb geopotential height (contours in m), vorticity (shaded in $10^4\ s^{-1}$), and wind (barbs) for (a) 00 UTC 29 December, (b) 00 UTC 30 December, and c) 12 UTC 30 December. NARR sea-level pressure (contours in mb) and 10-m wind (barbs) for, (d) 00 UTC 29 December, (e) 00 UTC 30 December, and (f) 12 UTC 30 December. All winds in knots.....	48

Figure 10	SSM/I passes of IWV (mm) from (a) 03 UTC 30 December, 2005, (b) 03 UTC 31 December, 2005, and (c) 15 UTC 31 December, 2005. Corresponding WRF simulated IWV (mm) from CTRL run for (d) 03 UTC 30 December, 2005, (e) 03 UTC 31 December, 2005, and (f) 15 UTC 31 December, 2005. Dark regions are areas not covered by ascending and descending satellite passes. Source: Remote Sensing Systems SSM/I data.	49
Figure 11	NARR 925 mb equivalent potential temperature (contours in K) and wind (barbs in knots) at (a) 00 UTC 29 December, (b) 00 UTC 30 December, and (c) 12 UTC 30 December. (d), (e), and (f) for the same times but for the WRF CTRL simulation.	50
Figure 12	Upper air sounding from Oakland, CA at (a) 00 UTC 29 December, (b) 00 UTC 30 December, (c) 12 UTC 30 December, and (d) 09 UTC 31 December.	51
Figure 13	Gridded observed 24 hour precipitation (mm) for (a) 12 UTC 29 Dec. to 12 UTC 30 Dec., 2005 and (b) 12 UTC 30 Dec. to 12 UTC 31 Dec., 2005. WRF CTRL run 24 hour precipitation for (c) same period as (a), and (d) same period as (b). Source of gridded precipitation: California-Nevada River Forecast Center (CNRFC). Gridded analysis area ends at the CNRFC region borders.	52
Figure 14	(a) Chico (CCO), CA wind profiler data for 30 Dec., 2005 up to 4 km. (b) WRF CTRL simulated winds below 600 mb at Chico, CA. Wind barbs are in knots, with time reading from right to left.	53
Figure 15	WRF CTRL run 500 mb geopotential heights (contours in m), vorticity (shaded in 10^4 s^{-1}) and wind (barbs in knots) at (a) 00 UTC 29 Dec., (b) 00 UTC 30 Dec., and (c) 12 UTC 30 Dec. WRF CTRL run sea-level pressure (contours in mb) and 10 m winds (barbs in m/s) at (d) 00 UTC 29 Dec., (e) 00 UTC 30 Dec., and (f) 12 UTC 30 Dec.	54
Figure 16	Comparison of GPS IWV (cm) values (cross-hatched lines) and WRF CTRL run simulated IWV values (solid lines in cm) at Cape Mendicino, Modesto, Chico, and Lost Hills.	55
Figure 17	Large scale moisture budget of moisture flux convergence, precipitation, and atmospheric storage for WRF CTRL run (a) 72 hour totals ($\text{mm } 72\text{hr}^{-1}$), and (b) 15 min rates ($\text{mm } 15\text{min}^{-1}$).	56
Figure 18	All plots from the WRF CTRL run: Sea-level pressure (contours in mb) and 10 meter winds (barbs in m s^{-1}) for (a) 00 UTC 30 Dec., and (b) 12 UTC 30 Dec., 2005. IWV (shaded) and $\sigma=.9205$ winds (arrows in m s^{-1}) for (c) 00 UTC 30 Dec., and (d) 12 UTC 30 Dec. (e) 72 hour total precipitation (mm).	57
Figure 19	All figures are CTRL WRF cross-sections of potential temperature (contours in K) and water vapor mixing ratio (shaded in g kg^{-1}): for cross-section Y (see Fig. 7) (a) 00 UTC 30 Dec., (b) 12 UTC 30	

	Dec., and (c) 00 UTC 31 Dec., 2005; for cross-section Z (d) 12 UTC 30 Dec., (e) 00 UTC 31 Dec., and (f) 12 UTC 31 Dec.	58
Figure 20	WRF CTRL time series of normalized moisture flux through sides (a) A-E (cross mountain flux), and (b) H, O, and P (valley flux). Flux values in $\text{kg m}^{-1} \text{s}^{-1}$	59
Figure 21	WRF CTRL run (mm) and $\sigma=.9205$ winds (m s^{-1}) at (a) 13 UTC 31 Dec., and (b) 17 UTC 31 Dec.	60
Figure 22	WRF 72 hour total water vapor flux ($\times 10^{12} \text{ kg 72hr}^{-1}$) through each box side (A-E, H, M, N, O, P) for the CTRL, NOCR, and NOTER runs.	61
Figure 23	WRF CTRL run 72 hour moisture budget of moisture flux convergence, precipitation, and atmospheric storage. Units are $\text{mm}/72\text{hr}$	62
Figure 24	All plots from the WRF NOCR run: Sea-level pressure (contours in mb) and 10 meter winds (barbs in m s^{-1}) for (a) 00 UTC 30 Dec., and (b) 12 UTC 30 Dec., 2005. IWV (shaded in mm) and $\sigma=.9205$ winds (arrows in m s^{-1}) for (c) 00 UTC 30 Dec., and (d) 12 UTC 30 Dec. (e) 72 hour total precipitation (mm).	63
Figure 25	All figures are NOCR WRF cross-sections of potential temperature (contours in K) and water vapor mixing ratio (shaded in g kg^{-1}): for cross-section Y (see Fig. 7) (a) 00 UTC 30 Dec., (b) 12 UTC 30 Dec., and (c) 00 UTC 31 Dec., 2005; for cross-section Z (d) 12 UTC 30 Dec., (e) 00 UTC 31 Dec., and (f) 12 UTC 31 Dec.	64
Figure 26	Comparison of normalized cross-mountain moisture flux through box sides A, B, C, D, and E for the CTRL, NOCR, and NOTER runs. Flux values in $\text{kg m}^{-1} \text{s}^{-1}$	65
Figure 27	NOCR time series of normalized cross-mountain moisture flux through sides A-E. Flux values in $\text{kg m}^{-1} \text{s}^{-1}$	66
Figure 28	Comparison of normalized moisture flux through box sides H, O, and P for the CTRL, NOCR, and NOTER runs. Flux values in $\text{kg m}^{-1} \text{s}^{-1}$	67
Figure 29	All plots from the WRF NOTER run: Sea-level pressure (contours in mb) and 10 meter winds (barbs in m s^{-1}) for (a) 00 UTC 30 Dec., and (b) 12 UTC 30 Dec., 2005. IWV (shaded in mm) and $\sigma=.9205$ winds (arrows in m s^{-1}) for (c) 00 UTC 30 Dec., and (d) 12 UTC 30 Dec. (e) 72 hour total precipitation (mm).	68
Figure 30	All figures are NOTER WRF cross-sections of potential temperature (contours in K) and water vapor mixing ratio (shaded in g kg^{-1}): for cross-section Y (see Fig. 7) (a) 00 UTC 30 Dec., (b) 12 UTC 30 Dec., and (c) 00 UTC 31 Dec., 2005; for cross-section Z (d) 12 UTC 30 Dec., (e) 00 UTC 31 Dec., and (f) 12 UTC 31 Dec.	69

Figure 31	Total 72 hour WRF simulated IWV (in cm) at GPS location from the WRF CTRL, NOTER, and NOCR simulations.	70
Figure 32	WRF 72 hour area average total precipitation (mm) in boxes 1-5 for the CTRL, NOTER, and NOCR simulations.	71

List of Tables

Table 1	Drying ratios from past studies for various mountain ranges; Alps (Smith et al. 2003), Andes (Smith and Evans 2007), and Oregon Cascades (Smith et al. 2005). The drying ratio for Northern California includes both the Coastal Range and Sierra Nevada range and is an average of 15 cases presented in Didlake (2007).	72
Table 2a	Summary of drying ratios for the CTRL, NOCR, and NOTER runs for box side A and the subsequent downstream sides.....	73
Table 2b	Summary of drying ratios for the CTRL, NOCR, and NOTER runs for box side B and the subsequent downstream sides.....	73
Table 2c	Summary of drying ratios for the CTRL, NOCR, and NOTER runs for box side D and the subsequent downstream side.	73

CHAPTER 1

INTRODUCTION

The transformation of an airmass as it moves over a mountain barrier determines the development and distribution of orographic precipitation. While it is well known that the moisture content of air in the lee of mountain ranges is significantly reduced from that of the upstream airmass, the detailed, three-dimensional interaction of moist flow and mountain barriers is often poorly characterized. The geographical location and orientation of the California Coastal Range and Sierra Nevada mountain ranges make them susceptible to the moist, tropical air associated with Pacific cyclones. As Pacific storm systems develop and approach the U.S. West Coast, moist air is transported essentially unaltered from the tropics into the mid-latitudes in the form of atmospheric rivers (Zhu and Newell 1998; Neiman et al. 2007). When this air impinges on the coastal ranges, it is lifted by the terrain, causing heavy orographically enhanced precipitation along the slopes of the Coastal Range and the Sierra Nevada Range (Fig. 1). The climatological distribution of heavy rainfall along the Coastal Mountain Range of California (Fig. 2) is consistent with the idealized model of precipitation along the upslope of a mountain range. There is also heavy precipitation along the Sierra Nevada Range, which lies in the lee of the Coastal Range. Precipitation amounts along the Sierra Nevada can often rival those along the coast. The simple two-dimensional conceptual model of airmass transformation suggests that the airmass in the Sacramento Valley should be drier and less likely to produce precipitation of such magnitude. Past studies, however,

have shown that air flow entering the Sacramento Valley is not as simple as a two-dimensional flow over the coastal range, and can originate from different locations through differential flow regimes caused by varying air mass stability characteristics (Galewsky and Sobel 2005).

The flux of moisture over and around the Coastal Range is a key to understanding the interaction of atmospheric rivers and the California topography. Current atmospheric water vapor observing systems are limited temporally over ocean, and spatially and temporally over land. Satellite passive microwave retrievals provide high-resolution observations over large areas, but are limited by orbital periods and are only available over ocean. The complex terrain of California also makes the placement of surface observing systems difficult. There is a need to fill in the gaps in water vapor observations with field studies and high resolution modeling to understand the origin and path of moisture as it relates to the precipitation in California.

The goal of this study is to investigate a landfalling atmospheric river impinging on the California coast and entering the Sacramento Valley. By doing so, we can gain an understanding of how the water vapor flux associated with an atmospheric river changes as it moves over mountain complex of northern California. Specifically, we will examine the 29-31 December 2005 storm. This storm had significant impacts in the region, is well documented, and has been analyzed in past studies (Reeves 2006; Didlake 2007; Neiman et al. 2007). This slow moving storm caused flooding along many rivers (Fig. 3), with major flooding along the Russian and Napa Rivers, several mudslides, and even flooding in the streets of San Francisco. The California Nevada River Forecast Center reported this storm to

be a major contributor to record precipitation in December 2005, which was the fourth wettest month on record in the region since 1920.

This paper is organized as follows. Chapter 2 provides further background on orographic precipitation and its influence on airmass transformation. Chapter 3 details the data sets used in the study. Chapter 4 describes the experimental design, including the numerical simulation setup, as well as the design and application of a moisture budget. Chapter 5 presents an overview of the 29-31 December 2005 storm. Chapter 6 describes the model verification. Chapter 7 presents the model moisture flux analysis and moisture budget results. Finally, conclusions are discussed in Chapter 8.

CHAPTER 2

BACKGROUND

2.1 Field projects

Over the last two decades, several field projects have provided invaluable insight into the development of heavy precipitation along the west coast of North America. The Sierra Cooperative Pilot Project (SCPP) in the 1980's, the California Land-falling Jets Experiment (CALJET) in the late 1990's, the Pacific Land-falling Jets Experiment (PACJET), the Coastal Observations and Simulation with Topography (COAST) I and II (Bond et al. 1997), and the Improvement of Microphysical Parameterization through Observational Verification Experiment (IMPROVE) I and II (Stoelinga et al. 2003) in 2000 and 2001, have all provided high temporal and spatial resolution data sets of Pacific storms. These projects were designed to examine the interaction among mid-latitude cyclones, strong moist flows, and the mountain ranges of California, Oregon, and Washington.

SCPP was the first to investigate how a wide spectrum of synoptic patterns and storms evolved as they interacted with the terrain (Heggli and Rauber 1998). Storms in a general west to southwesterly flow were found to be associated with heaviest precipitation. During COAST, observations of frontal systems approaching coastal topography provided insight into the modification of fronts and the development of barrier flows. IMPROVE II focused on the modification of fronts moving over the Cascade Mountain Range during the winter season, with an emphasis on microphysical processes. Prior to IMPROVE II, vertically

propagating gravity waves were known to influence vertical motion and precipitation structure above the mountain crest and just downstream (Bruitjes et al. 1994). One of the major findings of IMPROVE II was that the vertically propagating gravity wave can modify cloud structures and precipitation upstream of the mountain crest (Colle 2004, Smith and Barstard 2004, Garvert et al. 2007).

2.2 The low-level jet

CALJET and PACJET investigated the pre-frontal low level jet (LLJ) associated with Pacific storm systems. The LLJ, which forms to help restore thermal wind balance, can lead to extreme flooding when it transports moisture toward a mountain range (Buzzi et al. 1998; Doswell et al. 1998; Lin et al. 2001; Rotunno and Ferretti 2001; White et al. 2003; Ralph et al. 2004, 2005; Neiman et al. 2007). Ralph et al. (2004) used dropsonde and satellite data from CALJET to describe the characteristics of the LLJ and strong moisture transport associated with southwesterly flow. The baroclinicity of Pacific storms was found to enhance the prefrontal LLJ, which often forms in the pre-frontal warm sector ahead of mid-latitude cyclones near 900 mb and is responsible for the bulk of the moisture transport in Pacific storms. This confirmed the findings of Lackmann and Gyakum (1999), which revealed that the low-level southwesterly flow and moisture transport associated with Pacific storms is also enhanced by the interaction of Pacific low pressure systems and an anticyclone located downstream off the Southwest U.S. coast. Through piecewise potential vorticity inversion, the interaction of these features was found to strengthen the LLJ. Lackmann (2002) studied the formation and enhancement of the LLJ of a surface cyclone over the

south-central U.S. The potential vorticity maxima created by latent heating associated with diabatic processes along the cold front strengthens the pre-frontal low-level jet. Moisture transport is thus enhanced in the warm sector. The strength of the LLJ accompanying strong baroclinic systems over the Pacific Ocean is likely influenced in a similar fashion.

2.3 Atmospheric rivers

Collocated with the low-level jet is a narrow region, on the order of 1 km wide, of high water vapor content. This plume of moisture, also known as an atmospheric river (Zhu and Newell 1998), is similar to the warm conveyor belt present in many cyclones crossing the U.S (Carlson 1980; Browning 1990, Ralph et al. 2004). The majority of moisture in the atmospheric river is located below 2.25 km altitude, with horizontal dimensions of about 2000 km long and 1000 km wide (Neiman 2007), extending from the tropics into the mid-latitudes. There are typically four to five atmospheric rivers present across the Northern Hemisphere at any time, and these rivers are responsible for nearly 90% of the meridional moisture transport (Zhu and Newell 1998; Ralph et al. 2004). Atmospheric rivers play a key role in moisture availability for precipitation processes within mid-latitude cyclones, and the proximity of the mountainous terrain of the western U.S. to this moisture source is ideal for episodes of heavy orographic precipitation.

The findings of Zhu and Newell (1998) and subsequent field studies prompted Neiman et al. (2007) to perform the first climatology of atmospheric rivers over the Pacific Ocean, studying eight years of Special Sensor Microwave/Imager (SSM/I) data (1999-2006). Their study found that atmospheric rivers were more common in the summer than winter. In the

summer, atmospheric rivers were oriented more zonally with a less amplified mean flow compared to winter atmospheric rivers. Summertime atmospheric rivers typically contained more water vapor than those during the winter months. However, the storm dynamics of wintertime storms, specifically the LLJ, were stronger, and thus the wind field associated with the moisture transport was stronger than it was for summer storms. Wintertime systems were associated with a deep trough over the Pacific, with enhanced low-level baroclinicity and a polar cold front extending from northeast to southwest toward the tropics (Fig. 4). An atmospheric river can be seen as a region of large integrated water vapor located ahead of the front in the same region as the typical LLJ directed toward the California coast. The stronger flow suggests that the horizontal moisture flux associated with winter atmospheric rivers is stronger than in summer, leading to more orographic precipitation during the winter.

2.4 Airmass Transformation

2.4.1 Blocked vs. unblocked flow

The link between atmospheric rivers and flooding in California is now well established, which begs the question, “How is the moist airmass altered as it moves inland?” Understanding the hydrometeorological consequences of atmospheric rivers is an ongoing research topic. Galewsky and Sobel (2005) studied the 1997 New Year’s Flood, which was a representative case of a Pacific cyclone and attendant atmospheric river. Two distinct air masses were found to interact with the terrain and enter the Sacramento Valley by different methods (i.e., flow around versus flow over). Figure 5 describes the different ways air entered the Sacramento Valley in their case. Low θ_e air experienced blocking by the terrain

along the Coastal Ranges (Fig. 5a). High θ_e air associated with the atmospheric river was eventually able to ascend the northern Coastal Range due to the release of latent heat and destabilization (Fig. 5b), but was still partially blocked by the Sierra Nevada Range. The upvalley flow along the Sierras was instrumental in transporting moisture into the Sacramento Valley, where locally strong convergence along the northern windward slopes of the Sierras enhanced precipitation rates (Fig. 5c). These interactions of blocked and unblocked flow and the terrain may have significant consequences on the amount of moisture that is able to penetrate the Sacramento Valley, and in turn may influence how much precipitation falls along the windward Sierra slopes.

2.4.2 Drying ratios

Recent studies (Smith et al. 2003, 2005; Smith and Evans 2007) have addressed the concept of moisture depletion by elevated terrain. If moisture is forced to rise over a mountain barrier, the condensation of water vapor and conversion to precipitation will lead to decreased water vapor content downstream of the ridge. The amount of water vapor removed is related to the original amount of water vapor by the “drying ratio” (Smith et al. 2005)

$$Drying\ ratio = \frac{water\ vapor\ removed}{initial\ water\ vapor} \quad (1)$$

The drying ratio is a good parameter for evaluating moisture depletion, or airmass change, because it is simpler than precipitation efficiency since no knowledge of the vertical velocity of air is required. Calculations for different mountain ranges have found a spread of drying ratio values (Table 1), from 35% over the Alps (Smith et al. 2003) to 50% over the Andes (Smith and Evans 2007). Significant mountain ranges deplete, on average, at least one third of the original moisture of an impinging airmass. A more recent study by Didlake (2007) found an average drying ratio of around 30% over northern California, with a value as high as 66% for one individual storm. These California measurements are essentially two-dimensional, made by comparing moisture content upstream of the Coastal Range (Oakland, CA) and downstream of the Sierra Nevada range (Reno, NV). It is not yet known how moisture within the Sacramento Valley affects these drying ratio values (Ron Smith, personal communication 2007). The results of Galewsky and Sobel (2005) suggest that air is also able to enter the Sacramento Valley from the south. Thus, there is a need to understand the transport of moisture around the ranges, which could possibly lead to moistening of the depleted airmass as it descends over the Coastal Range and into the Sacramento Valley.

CHAPTER 3

DATA

Atmospheric water vapor is regularly measured by several types of instruments. Over the ocean, the Special Sensor Microwave Imagers (SSM/I) aboard the Defense Meteorological Satellite Program's (DMSP) polar orbiting satellites are able to retrieve Integrated Water Vapor (IWV) by measuring the thermal emission of both the earth's atmosphere and surface, and then relating them to the brightness temperature model function (Wentz 1997). Composite images from passes during the polar orbits of the SSM/I units are available roughly every 12 hours. Over land, water vapor is observed using near real-time GPS-Integrated Precipitable Water (IPW) measurements. These point measurements, maintained by the National Oceanic and Atmospheric Administration's Global Systems Division Ground Based GPS Meteorology Program, provide IPW, temperature, dew point, relative humidity, and pressure every 15 minutes at over 200 sites across the U.S. In this study, we use GPS IPW measurements in Cape Mendicino, Chico, Modesto, and Lost Hills (Fig. 1b). Even though the combination of these observations provides greater detail of the movement of water vapor over the globe than ever before, the current observing systems have several limitations, including coarse temporal sampling of about 12 hours by the polar orbiting satellites, a lack of SSM/I IWV measurements over land, and the coarse spatial distribution of surface-based observing systems. In this study, numerical model output is used to fill in

the gaps in observations and provide a more spatially and temporally continuous water vapor field.

The regional model used in this study is initialized with the North American Regional Reanalysis (NARR) dataset (Mesinger et al. 2006). The NARR data, a combination of the once operational ETA model and an assimilation data from various sources, is available on a 32 km grid every three hours. One of the more significant improvements of the NARR over global reanalysis datasets was made to the water budget (Mesinger et al. 2006), with several additional sources of moisture data assimilated. Of particular interest to this study, additional information about the moisture field over the oceans has been added to the dataset. NARR is able to resolve larger scale moisture transport associated mid-latitude cyclones, and in this study, the WRF model is used to downscale to smaller grid-spacing to resolve the horizontal and vertical gradients of moisture associated with atmospheric rivers.

CHAPTER 4

METHODOLOGY

4.1 Regional model design

We employ the Weather Research and Forecasting Model (WRF) Version 2.2 to obtain high resolution information on water vapor both over the ocean and land. WRF is a mesoscale numerical weather prediction model designed by the National Center for Atmospheric Research, the National Oceanic and Atmospheric Administration's National Center for Environmental Prediction and Forecast System's Laboratory, the Department of Defense's Air Force Weather Agency and Naval Research Laboratory, the Center for Analysis and Prediction of Storms at the University of Oklahoma, and the Federal Aviation Administration for both research and operational applications (Skamarock et al. 2005). This study utilizes the Advanced Research WRF (ARW) dynamical core, which is fully compressible, Euler non-hydrostatic, and uses terrain-following sigma (σ) coordinates. More information on the details of WRF ARW is available in Skamarock and Klemp (2007), Skamarock et al. (2006), and others.

One nested domain was used for the simulations (Fig. 6). Domain 1 used 27-km grid spacing with 150x130 grid points in the horizontal and 30s terrain resolution. Domain 2 used 9-km grid spacing with 241x196 grid points in the horizontal and 30s terrain resolution. Both domains used 45 vertical levels, distributed unevenly and maximized in the boundary layer. Time-steps of 108s and 36s were used for domains 1 and 2, respectively. North

American Regional Reanalysis (NARR), a 32-km gridded reanalysis dataset (Mesinger 2006) was used to initialize the model and update boundary conditions every three hours. The atmospheric river associated with the targeted storm made landfall on the northern California coast early on 30 December, so the model was initialized at 00 UTC on 29 December to allow for spin up. The simulations were run for 96 hours, through 00 UTC 2 January, 2006. The Kain-Fritsch cumulus parameterization scheme, Thompson microphysical parameterization scheme, and the Mellor-Yamada-Janjic boundary layer and surface layer parameterization schemes were each used for both domains. WRF Version 2.2 is updated to include a positive definite moisture transport scheme (Skamarock 2006), which will be discussed later.

Two sensitivity tests were performed, with the same initial conditions and model design as the control run (CTRL, Fig. 7a). The sensitivity tests isolate the effects of the terrain on blocking moisture transport by removing just the Coastal Range (NOCR run, Fig. 7b), and all terrain within the domain (NOTER run, Fig. 7c). It is hypothesized that the coastal range forces moisture to enter the Sacramento Valley through the Petaluma Gap. By removing all of the mountains, the impact of the entire west coast mountain complex on inland moisture transport can be examined. These runs are compared to the CTRL run and each other.

4.2 Moisture budget

The design of the moisture budget incorporated in this study was based on the spatial orientation of both the environmental phenomenon of interest, which was the atmospheric river, and the terrain of California. The goal was to examine to moisture flux into and out of

strategically placed boxes in order to quantify air mass transformation over the region. The following describes the calculations and design of two separate moisture budgets.

4.2.1 Integrated water vapor

It is critical that the model be able to represent the magnitude, as well as the timing of the rise and fall of IWV associated with the atmospheric river in order to verify the moisture fluxes directly associated with the atmospheric river. The model produces water vapor mixing ratios for each model level, which is then used to compute IWV (m) by the expression:

$$IWV = \frac{1}{\rho_w g} \int q_v dp \quad (2)$$

where g (m s^{-2}) is the gravitational acceleration, ρ_w is the density of water (1000 kg m^{-3}), q_v ($\text{kg}_{\text{water}} \text{ kg}^{-1}_{\text{air}}$) is the layer average water vapor mixing ratio between each model level, and dp (Pa) is the depth between each model level over which q_v is computed. This equation is similar to the computation for IPW, and IWV can be compared to IPW if both are calculated up to and through at least the troposphere (Paul Neiman, personal communication 2007). WRF IWV will hereafter be expressed in millimeters (mm) to compare to SSM/I IWV over ocean, and centimeters (cm) to compare to GPS IPW over land.

4.2.2 Horizontal Moisture Flux

The vertically integrated horizontal moisture flux ($\text{kg m}^{-1} \text{s}^{-1}$) at each grid point along a box side is computed with positive and negative flux values assigned following Fig. 8a, using

$$Q_{Flux} = \frac{1}{g} \int q_v V_n dp \quad (3)$$

where g , q_v , and dp are defined in Chapter 4.2.1, and V_n is the layer average horizontal wind (m s^{-1}) normal to a budget box side over dp . The flux of all other hydrometeor species, defined as q_t , including ice, cloud water, cloud ice, graupel, snow, and rain, is computed using the same method and substituting q_t for q_v in (3). Moisture flux is computed every 15 minutes and the flux is assumed to be constant during that 15 minutes.

4.2.3 Regional scale budget

A regional scale moisture budget is computed for a region approximately two-thirds the size of the model 9 km inner domain (Fig. 6) to test the horizontal moisture flux computation described in Chapter 4.2.2 with the model moisture fields. The conservation equation for moisture

$$\frac{\partial S}{\partial t} = F + E - P \quad (4)$$

is evaluated using a 15 minute time step, where S is the storage of moisture in the atmosphere as water vapor and other hydrometeors, F is the flux convergence of moisture, E is evaporation, and P is the precipitation fallout within the budget box. Here, all terms on the right side of (4) are expressed in $\text{mm } 15\text{min}^{-1}$ (which is equivalent to the units of mass flux $\text{kg m}^{-2} \text{s}^{-1}$) to facilitate comparisons to IWV measurements. In addition, all right side terms are explicitly output from the model, with the exception of the contribution vertically-integrated horizontal moisture flux (3).

There are two main components of the total moisture flux convergence in this budget; the vertically-integrated horizontal moisture flux (3) and the surface moisture flux. The contribution due to the vertically-integrated horizontal moisture flux within a defined area can be computed using the line integral around the budget area,

$$F_{horiz} = \frac{\rho_w}{A} \oint Q_{Flux} \cdot dl \quad (5)$$

where A is the area of the box (m^2), ρ_w is the density of water (1000 kg m^{-3}), Q_{Flux} is defined in (3) and converted to a 15 minute flux ($\text{kg m}^{-1} 15\text{min}^{-1}$), and dl is the length of a box side (m). The horizontal winds used in (5) are normal to the box sides, or the u and v components of the wind. Flux into the box on the lateral sides is defined to be positive flux and flux out of the box to be negative. It is assumed that no moisture exits through the top of the box, and is a reasonable assumption with the top of the box at 100mb.

The surface moisture flux F_{sfc} is directly output from the model in units of $\text{mm } 15\text{min}^{-1}$, and over the entire surface of a box can be expressed as an area average by

$$F_{sfc} = \frac{1}{n} \sum_{i=1}^n F_{sfc_i} \quad (6)$$

where n is the number of grid cells used within the budget domain, and F_{sfc} is the model surface moisture flux ($\text{mm } 15\text{min}^{-1}$). Positive surface moisture flux is defined as upward, or into the box.

Similarly, the box area average precipitation is computed by

$$P = \frac{1}{n} \sum_{i=1}^n P_i \quad (7)$$

where n is the number of grid cells used within the budget domain, and P is the model precipitation (mm). Precipitation from the model output is a storm accumulated total, and considering the change in storm accumulated precipitation at every output time gives a rain rate in ($\text{mm } 15\text{min}^{-1}$). Finally, evaporation (E) is not explicitly computed in this study, as the term is accounted for in surface fluxes (surface evaporation) and the flux of q_v into and out of the budget box.

4.2.4. Small scale budgets

A set of moisture budgets were computed on the horizontal scale of the mountain ranges using the same mathematical methodology described above. In total, five boxes were placed in locations that would capture moisture flux offshore, along the coast, and inland, and to diagnose air mass transformation over the key areas. In order to accurately capture the effects of the mountain range, the boxes were oriented parallel to the main axis of the Sierra Nevada range, which was approximated to be 26 degrees west of north. The terrain parallel box sides are also perpendicular to the along-flow axis of the atmospheric river (Fig. 8b; labels A-E, M, N) and were designed to capture specific aspects of the moisture transport; A) the bulk transport of the atmospheric river, B) the change, if any, of moisture prior to landfall, C) the change of moisture over the Coastal Range, D) the change of moisture across the Sacramento Valley, E) the effect of the Sierra Nevada Range on the moisture, M) the amount of moisture entering through the Petaluma Gap, and N) the effect of the Sierra Nevada Range on the moisture entering through M. In this study, we focus on sides A-E. The other nine sides closed the boxes to complete the moisture budget on its lateral sides, with sides H and P designed to measure the amount of moisture entering the valley from the south and exiting the valley to the north, respectively. Side O represents moisture flux in the San Joaquin Valley.

CHAPTER 5

29-31 December 2005 Case Description

The large scale flow during the December 29-31, 2005 storm was characterized by a longwave trough over the Pacific Ocean (Fig. 9 a-c), with an occluding surface cyclone in the Gulf of Alaska (Fig. 9d). At 00 UTC 30 December, a cold front and low pressure trough extended from the Washington and Oregon coasts to the southwest into the central Pacific (Fig. 9e). SSM/I imagery from the morning of 30 December (Fig. 10a) revealed a broad, ill-defined area of moisture off the west coast, with moisture extending northwestward into the Gulf of Alaska near the main low pressure center. Later on 30 December at 12 UTC, a surface wave was beginning to develop along the original occluded front (Fig. 9f). The aforementioned broad area of moisture became focused into a narrow and well-defined atmospheric river by 03 UTC 31 December (Fig. 10b), noted by strong gradient of moisture across the atmospheric river. The atmospheric river was directed in the climatological direction of southwest to northeast, towards the California coast. An analysis of the low-level θ_e field (Fig. 11) shows the evolution of the low-level warm front as a strong gradient in θ_e , which developed at the nose of the atmospheric river as it approached the California coast. The warm front was weak early in the event, but as the storm developed (Fig. 11a) the warm front strengthened as the atmospheric river became more defined and neared the coast (Fig. 11b and 11c). Strengthening of the warm front may have been aided by evaporational cooling. The strengthening of the warm front was a factor in the how the atmospheric river

interacted with the coastal terrain, and will be discussed in subsequent chapters. Along the coast, the airmass was initially dry (Fig. 12a), but as the atmospheric river approached, moisture along the warm front caused gradual moistening, first at mid-levels near the 700 hPa (Fig. 12b), then later at 850 hPa (Fig. 12c). It was during the passage of the warm front and atmospheric river, aided by the pre-frontal LLJ (Fig. 12d), that the heaviest precipitation transitioned from along the Coastal range (Fig. 13a) to the windward slopes of the Sierras (Fig. 13b), with some locations along the windward slopes of the Coastal Range receiving over 6 inches (>150 mm) of precipitation in a 24 hour period. As the system moved to the east and made landfall, cold front moved further south and enhanced the moisture gradient across the atmospheric river, causing the river to narrow (Fig. 10b and 10c). The front and moisture continued to move south down the California coast on 31 December, causing a shift in the heaviest precipitation totals from the north to south along the Sierras (not shown) on 1 January, 2006.

Barrier jets are known to occur along the Sierra Nevadas (Parish 1982). Air flow impinging on mountain ranges is slowed as it rises up the slopes. The mass convergence along the slopes causes an increase in pressure and strengthens the pressure gradient. The airflow along the barrier speeds up in response to the pressure gradient, and a barrier jet forms. The low-level flow in the Sacramento Valley turned to southeasterly at 02 UTC 30 December (Fig. 14a), and steadily strengthened through the next several hours. The barrier jet was strongest around 18 UTC 30 December at 1km in altitude. The timing of the barrier jet corresponded to the landfall of the atmospheric river, and is likely to have contributed to the transport of moisture within the Sacramento Valley.

CHAPTER 6

MODEL VERIFICATION

6.1 Synoptic flow and atmospheric river

The WRF model was able to simulate the overall development and movement of the storm system. The upper-level (Fig. 15a-c) and surface flow (Fig. 15d-e) compared well to the observed flow. A comparison of the SSM/I imagery of IWV with model simulated IWV shows that the initialization and simulation of the moisture field was also representative (Fig. 10). The atmospheric river simulated by the model was remarkably similar to the observed river, with core IWV values within a few millimeters of the observed values. It is also noteworthy that the simulation also represents the evolution of the moisture from a broad plume to a narrow, focused river of moisture (Fig. 10). While some studies have investigated the strong moisture transport over the eastern Pacific Ocean (Galewsky and Sobel 2005, Lackmann and Gyakum 1999), to the author's knowledge, this is the first study to test the ability of a numerical model to simulate the 3-D characteristics and evolution of an atmospheric river as it makes landfall.

Having a good simulation of the atmospheric river over the ocean is essential to the validation of the model run and investigation of the approach of moisture to the coast. It is also necessary to validate the model by verifying the representation of moisture over land. Since SSM/I imaging techniques are only valid over the ocean, point values of GPS-IWV are used to verify the rise and fall of moisture as the storm passes. Figure 16 reveals that the

observed and model simulated IWV agree very well. The model was able to represent the rise and fall of moisture, as well as the relative magnitudes of moisture associated with the airmasses at each location. Some GPS-IWV data were not available on 31 December, but the model results show a steady decline of IWV as the system passes.

6.2 The barrier jet

The barrier jet that develops along the slopes of the Sierras within the Sacramento Valley is also represented in the WRF simulation (Fig. 14b). The low-level winds turn to southeasterly after 03 UTC 30 December, and strengthen to 40 knots at 21 UTC 30 December. Observations show a barrier jet with max wind speeds of 50 knots. The Chico profiler has higher resolution in the lowest 4 km than the WRF simulation, and therefore may be able to better resolve the localized maximum in this case. However, the directional development and strengthening of the simulated wind field is indicative of a barrier jet.

6.3 Precipitation

Precipitation is often difficult to measure in complex terrain, mainly because of difficulties in instrument siting, maintenance, and representativeness issues (Strangeways 1996). Gridded data (Fig 13a and 13b) and rain gauge reports (not shown) agree well with one another, and a comparison of a River Forecast Center gridded mosaic and the WRF simulated total precipitation from the most active 24 hour period of the event (Fig. 13c and 13d) shows a well simulated precipitation distribution overall. The model captures the precipitation that formed along the windward slopes of the Coastal Range, as well as along

the windward Sierra slopes. The model produces a maximum of precipitation along the Coastal Range near 40°N, 124°W that is up to 4 inches higher than the observed precipitation. This feature is highly localized, and was investigated through a series of model simulations with varying physics, each producing the same bullseye of precipitation. It is possible that the maximum is related to a terrain feature in the model terrain package, but since the feature covers such a small area in the domain, we do not feel it will significantly impact the results of the broader water vapor analysis. A second maximum of precipitation occurs along the slopes of the Siskiyou Mountains at the northern extent of the Sacramento Valley.

6.4 Regional Scale Budget

The results of the regional scale moisture budget are shown in Fig. 17a. The total precipitation is slightly less than the total water vapor convergence (Fig. 17a). The total moisture convergence is dominated by the q_v flux convergence on the lateral sides of the box and the surface. The q_t flux is nearly negligible. This is likely being attributable to the production of these hydrometeors occurring almost completely within the box. The storage of atmospheric moisture, or the moisture added during the 72 hour run, is less than 10%, and analysis of the final IWV suggest that much of the residual moisture is located within the Sacramento Valley (not shown). The evolution of the flux convergence and precipitation fall out (Fig. 17b) reveals a strong convergence of water vapor early in the run, with about a six hour time lag before precipitation rates begin to increase.

CHAPTER 7

RESULTS

7.1 Positive-definite moisture transport

The transport of scalar quantities, in this case the mixing ratios of water vapor and hydrometeors, creates complications when considered in more than one dimension, where negative mixing ratios are often set to zero. This has significant implications near large moisture gradients and can lead to significant errors in the evaluation of moisture transport from 3D model output. Version 2.2 of the WRF model was updated to include a positive-definite moisture transport scheme (PDMTS, Skamarock 2006), which is critical to the closing of the moisture budget of the WRF model (Brian Colle and Scott Braun, personal communication 2007). The following results are based on model simulations with a PDMTS scheme turned on. Initial simulations had been run with WRF Version 2.1.2, which had a large discrepancy between total precipitation and water vapor convergence. Differences in model fields at individual times between runs with and without a PDMTS were typically small and difficult to notice (not shown). However, these small differences at each model time step became significant over the duration of the run and were a major factor in the moisture budget closure.

7.2 CTRL

7.2.1 Moisture flux analysis

A summary of the CTRL run is presented in Figure 18. Strong southwesterly low-level flow is evident between the approaching storm system and an anticyclone anchored off the southern California coast (Figs. 18a and 18b). Initially, at 00 UTC 30 December, the atmospheric river is broad and fans out at the warm front (Fig. 18c). The low-level winds are blocked which enhances the wind shift at the warm front and helps to keep the low-level moisture offshore. Some of the offshore moisture is lifted up and over the warm front (Fig. 19a). By 12 UTC, the low-level moisture impinges on the coast (Fig. 19b), and the low-level winds are able to ascend the Coastal Range (Fig. 18d). By 00 UTC 30 December, some of the moisture is able to ascend to the crest of the Coastal Range (Fig. 19c). The moisture crossing the Coastal Range can first be seen in the Sacramento Valley as an elevated region of moisture (Fig. 19e) that does not reach the surface. Eventually, the atmospheric river narrows and is pushed south by the advancing cold front (Fig. 18d). At the same time, a layer of moisture closer to the surface with higher mixing ratios than air crossing the Coastal Range, advances up the Sacramento Valley from the south (Fig. 19f). The simulated storm total precipitation presented in Figure 18e reflects the orographic lifting that occurs along the Coastal Range, as well as moist air being lifted within the Sacramento Valley along the slopes of the Siskiyou.

The flow of moisture associated with the atmospheric river in terms of fluxes offshore, near the coast, and within the Sacramento Valley is described by a time series of the moisture flux results for sides A-E (see Fig. 8 for reference) in (Fig. 20a). This set of box sides

represents the flux perpendicular to the mountains and along the orientation of the atmospheric river. The approach of the atmospheric river is evident in the rise in moisture flux through the offshore sides (A and B), which peaks around 00 UTC 31 December. A small reduction occurs from A to B and may be attributable to conversion to precipitation as air is lifted over the warm front (Fig. 19a). The moisture flux through sides C, D, and E shows passage of the atmospheric river downstream of the Coastal Range and Sierras. The peak values are much less than those upwind of the mountain ranges. Overall, there is a general reduction in moisture flux values from west to east with the greatest reduction between B and C, which lie on each side of the Coastal Range. This large reduction is evidence that the Coastal Range is removing the more moisture from the atmosphere than any of the other boxes. The change from C to D across the Sacramento Valley is small, as moisture is added to the valley from the south. Flux values are lowest through line E, and a calculation of fractional reduction from A to E suggests a total decrease of 55% (Table 2a). The reduction of moisture flux from B to E (Table 2b), which is analogous to the two-dimensional drying ratio presented earlier, is roughly 49% and consistent with previous studies (Table 1). The Coastal Range and Sierras remove about 28% and 25%, respectively (Table 2c).

The flux through sides H, O and P represents the along valley flux (Fig. 20). The flux is down-valley (negative values) until 12 UTC 30 December for H and P. The flux then becomes up-valley (positive) in the Sacramento Valley, while remaining down-valley in the San Joaquin through 21 UTC 30 December, suggesting flow splitting as the flow impinges on the Sierras. Frontal passage can be seen most strongly through side P around 03 UTC 31

December, as moisture flux values fall dramatically for about 2 hours. A second surge of moisture occurs soon after, indicative of a strong flux of moisture up the Sacramento Valley. The peak of the moisture flux through sides H and P occurs around 12 UTC 31 December, just after the atmospheric river passes by the Petaluma Gap (Fig. 21a), and moisture is able to flow into the Sacramento Valley unimpeded. The magnitude of the peak up valley flux ($\sim 300 \text{ kg m}^{-1} \text{ s}^{-1}$ through side H) is slightly more than half of the cross Sacramento Valley flux through C and D ($\sim 500 \text{ kg m}^{-1} \text{ s}^{-1}$). The time-integrated flux across H makes up 27% of the difference between B and C (Figure 22). As the atmospheric river moves further south, the up-valley flux through side O increases and peaks around 18 UTC 31 December. This suggest that moisture is able to ascend the Santa Lucia range, enter the valley, and is then deflected northward by the higher Sierra Nevada (Fig. 21b) However, the magnitude of the San Joaquin Valley flux (side O) never reaches the value of the Sacramento Valley fluxes at side H. Finally, all fluxes decrease sharply behind the atmospheric river, as the cold front forces the moisture source southward.

7.2.2. Small scale budget

The small scale moisture budget results for each box are presented in Figure 23. The smaller boxes show a consistent relationship between moisture convergence and precipitation in general, as moisture convergence values rival total precipitation. However, there are a few significant inconsistencies, especially in the valleys. Offshore (Box 1) the amount of precipitation in is slightly greater than the total convergence. Just downstream, over the Coastal Range (Box 2), the precipitation fallout is largest of all the boxes, and as expected,

the moisture convergence is also greatest. In this box, the atmospheric river impinges on the mountain range and a large amount falls out as precipitation, causing a significant reduction of moisture that is able to exit the box downstream of the barrier. This is qualitatively consistent with the conversion of moisture excess to precipitation. Within the Sacramento Valley (Box C), the amount of q_v convergence is less than the amount of precipitation. A possible explanation for the difference in convergence and precipitation is the layout of Box 3. The northwestern most corner of the box appears to overlap a portion of an area with heavy precipitation (see Fig. 8 and Fig. 13c). This is a result of the rectangular box layout within the complex terrain. The eastern side of Box 3 is parallel to the Sierra slopes, where significant precipitation occurs. This has an on the budget totals, as there is a large amount of q_t flux out of the box due to lighter hydrometeors leaving the box on the downstream side. Box 4 over the Sierras shows a larger convergence of water vapor and 81% of the area average precipitation of the Coastal Range. The excess moisture convergence may again be related to the flux of hydrometeors into Box 4. Finally, Box 5 shows much less moisture convergence than precipitation. Like Box 3, the eastern side of Box 5 lies along the windward Sierra slopes, where precipitation generation and the flux of hydrometeors downwind may cause a flux divergence that contaminates the total convergence. Overall, storage values are greatest over the Sierras, within the southern Sacramento Valley and in the San Joaquin Valley, where residual water vapor from the atmospheric river is largest.

7.3 NOCR

The effects of the Coastal Range are isolated in the NOCR run (Fig. 24). The low-level flow is still southwesterly ahead of the approaching storm, with an anticyclone off the southern California coast (Fig. 24a and 24b). The atmospheric river approaches as a broad area of moisture (Fig. 24c) which is lifted along the warm front (Fig. 25a). With no Coastal Range topography, the low-level flow is not blocked, and the low-level moisture is able to advance more quickly onshore (Fig. 25b and 25c). The transport of moisture into the Sacramento Valley is primarily from the west in the NOCR run (Fig. 25d-f). The atmospheric river is able to penetrate inland to the Sierras, where the flow is deflected to the north towards the Siskiyou. At the base of the Siskiyou the southerly flow converges with moisture that is transported eastward along the modified base of Siskiyou terrain (Fig. 24d).

Precipitation totals from the NOCR run are presented in Figure 24e. The precipitation along the coast is much less with the Coastal Range removed. The highest precipitation values are instead located near the concavity formed where the Siskiyou and Sierras meet. Here moist air from directly off the Pacific and air deflected northward by the Sierras persistently converges throughout the run, leading to enhanced precipitation over a small area. Much like the CTRL run, most of the precipitation appears to be driven by orographic effects and locked to the areas of sharp elevation and orographically forced convergence zones.

The offshore fluxes are nearly identical in the NOCR and CTRL runs (Fig. 26a). Closer to the coast, the flux is higher (Fig. 26b) in NOCR, but there is still a reduction in the flux from A to B as the moisture passes over the warm front (Fig. 27). More moisture from the

atmospheric river (IWV > 30mm) is able to reach the coast and penetrate further inland than in the CTRL run (Fig. 24d). However, the moisture and low-level flow is still blocked by the Sierras and forced northward. The difference in the CTRL and NOCR water vapor fluxes through side C is the largest of any side (Fig. 26c). The peak of the flux through side C occurs at the same time in both runs, but the NOCR flux is over $100 \text{ kg m}^{-1} \text{ s}^{-1}$ higher near 00 UTC 31 December. Inland, there is more flux through side D in the NOCR run about $50 \text{ kg m}^{-1} \text{ s}^{-1}$ more at the peak (Fig. 26d). The flux through side E shows almost no difference between the CTRL and NOCR runs (Fig. 26e), implying nearly equal depletion by the time the air mass reaches the lee of the Sierras in both runs.

The along-valley fluxes are very similar through the southernmost box sides (Fig. 28a and 28b, Fig. 22) in the NOCR run. The up-valley fluxes are similar in magnitude because the low-level flow is still blocked by the Sierras and forced northward in both runs (Fig. 24d). There is a substantial increase in moisture flux through the side P at the base of the Siskiyou in the NOCR run (Fig. 28). Moisture that is able to enter the valley where the Coastal Range used to be is now transported further north than was the case in the CTRL run (Fig. 25d-f).

7.4 NOTER

A summary of the NOTER run is shown in Figure 29. The effects of removing all terrain from the CTRL run were to cause a more constant flux through the boxes, and reduce the total precipitation significantly. The atmospheric river that developed was weaker off shore than in the CTRL run, but remained steady at around $700 \text{ kg m}^{-1} \text{ s}^{-1}$ through B-E (Fig. 26). The formation of the storm system appears to be different enough from the CTRL run to

impact the strength of the LLJ, and therefore, to alter the flux over the ocean. This is consistent with the results of Lackmann and Gyakum (1999). In their findings, an anticyclone located off the California coast southeast of the approaching storm system played a small but important role in focusing the moisture transport of the approaching storm system. In the CTRL run presented in Chapter 7.2, there was indeed an anticyclone located off the California coast (Fig. 18b). However, in the NOTER run, this anticyclone was shifted east over southern California (29b). Such a change in the large scale flow appears to have the effect of reducing the moisture flux offshore by $\sim 200 \text{ kg m}^{-1} \text{ s}^{-1}$. The bulk of the moisture reaches far inland into Nevada (Fig. 29d), unhindered by any terrain (Fig. 30a-c), and peaks several hours later than in the CTRL run (Fig. 26d), before retreating south with the cold front. As was the case in the NOCR run, there is no Coastal Range to block moisture (and no Sierras in the NOTER run), allowing the atmospheric river to move inland uniformly.

While the flux through sides A-E are unchanged, the flux through M and N are significantly greater than A-E. M and N are located to the south of A-E, which suggests that the moisture flux of the atmospheric river becomes stronger as the atmospheric river moves down the coast. This feature was alluded to in the case description, where it was noted that the atmospheric river narrowed as the cold front pushed south. A strengthening of the baroclinicity due to the cold front surging south would help to strengthen the LLJ, although this feature is not quantified in this study.

Moisture flux through sides H, O, and P remain negative through the entire run (Fig. 28). In this case, negative values are not representative of down-valley flux, but instead are a

result of the orientation of the box sides and a westerly flow. The 72 hour precipitation total from the NOTER run (Fig. 29e) shows an area of increased precipitation along the coast and a generally uniform precipitation distribution inland. Frictional convergence appears to enhance precipitation along the coast, although the effect is small.

7.5 IWV totals

It has already been shown that the advancement of the atmospheric river is impeded by the Coastal Range. The moisture is either blocked and forced around the barrier, or reduced as it ascends the slopes. To determine the overall sensitivity to terrain, we examine the modeled storm total IWV for the CTRL run at each of our four GPS sites for the entire 72 hours of the model run, and compare to the storm total IWV for the sensitivity runs (Fig. 31). Assuming IWV is essentially constant over a site for 15 minutes, these values represent a sum of IWV from each model output during the run. As discussed in Chapter 7.4, the strength of the atmospheric river is weaker in the NOTER run, which causes IWV values to be smaller at each site.

The change in IWV at the four GPS locations related to removing the Coastal Range is very small overall. The location of Cape Mendicino along the coast is such that removing the Coastal Range does not affect the total moisture that flows over the site. The mountains that remained in the NOCR run appear to keep the atmospheric river from moving inland until it is south of Cape Mendicino (Fig. 24d). The most significant change occurs at Chico, where about 20 cm more water vapor passes over the site in the NOCR run. Chico is located within the Sacramento Valley, and would be exposed to more moisture with no Coastal

Range, but, as shown in Chapter 7.2, a considerable amount is still able to flow around in the CTRL run. At Modesto, there is again very little change in total IWV. Modesto lies south of the Petaluma gap and is exposed to moisture that enters through the gap that is initially deflected southward, and by moisture that flows over the Santa Lucia range and flows northward later in the event. Lost Hills is located at the southern end of the San Joaquin Valley. Moisture reaching Lost Hills is also unaffected by removing the the Coast Range. If the Santa Lucia Range was removed, there would likely be more impact at Modesto and Lost Hills.

7.6 Moisture flux totals

Although the totals at the GPS-IWV locations are similar between the CTRL and NOCR runs, a comparison of the storm total moisture fluxes (Fig. 22) through each of the box sides emphasizes that removing the Coastal Range has a net effect to increase the moisture fluxes perpendicular to the mountain ranges (B-E). Offshore (A), removing the Coastal Range has almost no effect. Moisture flux in NOCR increases upstream of the Coastal Range (B and in the lee of the range in C). Across the Sacramento Valley, the total flux through side D in the NOCR run is also larger than in the CTRL run. The difference in side D is not as large as the difference through side C, which lies on the lee side of the Coastal Range. In the CTRL run, moisture is able to enter the Sacramento Valley from the south through the Petaluma Gap, supplying moisture between sides C and D, and thus reducing sensitivity of the flux through side D to removing the Coastal Range. Total moisture flux through side E downstream of the Sierra crest shows almost no change between the CTRL and NOCR runs.

Side M is an extension of side C along the lee slopes of the Coastal Range, but reaches across the Petaluma Gap. The storm total flux through the Petaluma Gap (M) is slightly larger than the flux impinging on the Coastal Range (B), suggesting that a considerable portion of the atmospheric river is forced around the barrier. The flux through M is much larger than the upvalley flux through H, as a portion of the moisture is lifted up the Sierra slopes and converted to precipitation. The rest is deflected upvalley along the slopes.

The total along valley fluxes (H, O, and P in Fig. 22) is consistent with the time series shown earlier (Fig. 28). There is almost no effect in removing the Coastal range on the flux through sides H and O. The flow is still deflected by the Sierras in both the CTRL and NOCR, leading to similar fluxes throughout the event. There is a large increase in flux through side P in the NOCR run, where moisture is able to penetrate directly into of the Sacramento Valley before being deflected northward by the Sierras (Fig. 24).

7.7 Precipitation totals

Storm total precipitation values for individual boxes quantify the precipitation analyses described earlier. Comparing the precipitation totals for the NOCR run to the CTRL run reveals little change in Box 1 (Fig. 32b). However, the precipitation in Box 2 is significantly reduced without the Coastal Range. Precipitation totals in Boxes 3 and 4 rise in the NOCR run, with more moisture reaching the slopes of the Sierras (Fig. 22). Box 5 precipitation remains nearly unchanged for each run.

The NOTER run produces much less precipitation than the other two runs. With no elevated terrain to force ascent, precipitation is limited mainly to synoptic and frontal

forcing. When the precipitation totals are normalized by the area of the boxes (not shown), there is more precipitation within Box 2 than any other box in the NOTER run. This precipitation occurs along the coast at the boundary between ocean and land. Frictional convergence appears to be the forcing for this enhancement of precipitation.

CHAPTER 8

CONCLUSIONS

Atmospheric rivers accompanying Pacific storm systems play an important role in supplying moisture to the U.S West Coast. Heavy precipitation associated with these systems falls not only along the west-facing slopes of the Coastal Range, which is subject to the direct landfall of the atmospheric rivers, but also along the windward slopes of the interior mountains. Moisture transport into the Sacramento Valley is a critical feature in understanding the impacts of land-falling atmospheric rivers and the aforementioned precipitation features. The 29-31 December, 2005 storm brought heavy rain and flooding to much of northern California. Simulations of the storm using the WRF model were able to realistically resolve the structure and strength of the atmospheric river over ocean and land. The atmospheric river strengthened and became more focused as the storm approached the West Coast, and made landfall along the northern California coast. The analysis of fluxes presented in chapter 7.2.1 provided valuable insight into the transport of water vapor toward the coast and into the Sacramento Valley.

The atmospheric river was slowly lifted along isentropic surfaces offshore before interacting with the coastal topography. Over land, the Coastal Range caused a significant reduction in moisture flux of air entering the Sacramento Valley after crossing the terrain. A simulation with no Coastal Range verified this reduction by producing an increased moisture flux immediately downstream of the removed terrain. The moisture that enters by flowing

around the Coastal range and through the Petaluma Gap helps to compensate for the moisture depleted by the westerly flow over the Coastal Range. Removing the Coastal Range does change either the amount of moisture that enters where the Petaluma Gap would be located or the deflection of low-level moisture northward by the Sierras..

The up-valley moisture flux at the base of the Siskiyou is comparable to the flux of moisture entering the Sacramento Valley through the Petaluma Gap, suggesting that the along valley flow is able to travel up the Sacramento Valley nearly unchanged before reaching the Siskiyou. The barrier jet along the Sierras appears to drive this flux of moisture northward deep into the Sacramento Valley. When the Coastal Range is removed, the up-valley flux near the base of the Siskiyou is much larger than in the run with coastal topography. Not surprisingly, the Coastal Range plays a key role in how much moisture reaches the Siskiyou.

On the downwind side of the Sierras near Reno, the moisture flux is found to be 49% of the moisture flux on the windward side of the Coastal Range, and nearly 55% less than the moisture flux well offshore (Table 2). The Coastal Range itself is found to cause a drying ratio of 25%, While the Sierras account for 30%. The regional drying ratio, or that across the entire mountain complex, does not change significantly when the Coastal Range is removed. The amount of moisture that flows around the Coastal Range replenishes part of the moisture depleted over the Coastal Range, and then the Sierras remove the similar amounts of moisture in both cases.

When all terrain over the Western U.S. is removed, the synoptic flow develops with a low-level anticyclone located much further east than observed. The low-level flow between

the approaching cyclone and this anticyclone is much weaker, leading to a weaker atmospheric river. Moisture fluxes in a simulation with no terrain are much weaker than in the control simulation. The atmospheric river is able to reach far inland into Nevada, and moisture reduction near the coast is minimal, due mainly to conversion to precipitation by frictional convergence along the coast.

The scenario presented in this study represents the impact of the California mountains ranges on atmospheric rivers for one case. It presents a plausible representation of how moisture may enter the Sacramento Valley in similar cases. The structure of the mountain complex in Northern California creates a scenario where moisture impinges on the Coastal Range and is converted to precipitation through orographic lifting. Some of the moisture is able to make it over the range and descend into the valley. A significant amount of moisture moves around the topography and enters the valley through the Petaluma gap. The moist air is then blocked by the Sierras and forced northward up the valley, where it often converges with air that is able to ascend the coastal range. The majority of the moisture entering the valley is eventually converted to precipitation along the mountain slopes as less than half of the original moisture over the ocean makes it to the lee of the Sierras.

CHAPTER 9

FUTURE WORK

The results presented apply to the 29-31 December, 2005 Pacific storm. The conclusions drawn from the moisture budget and moisture flux analysis describe the transport of moisture over and around the coastal barriers and into the Sacramento Valley. The results of one case study are not considered to be sufficiently robust to apply to every case. These results likely describe aspects of the basic path of water vapor into the Sacramento Valley under similar synoptic conditions. Analysis of several cases is needed to more accurately quantify the role of the Coastal Range in moisture depletion across a range of synoptic conditions

A potential extension of this analysis involves the sensitivity of off-shore blocking and the moisture budget to diabatic cooling. Evaporational cooling could enhance the stability of air on the windward side of the coastal range. This stable layer could act similar to topography and lift air further upstream of the slopes. A sensitivity run with evaporational cooling turned off is needed to test this hypothesis. In addition, a sensitivity run with no surface friction is needed to investigate the enhanced precipitation along the coast in the NOTER run.

FIGURES

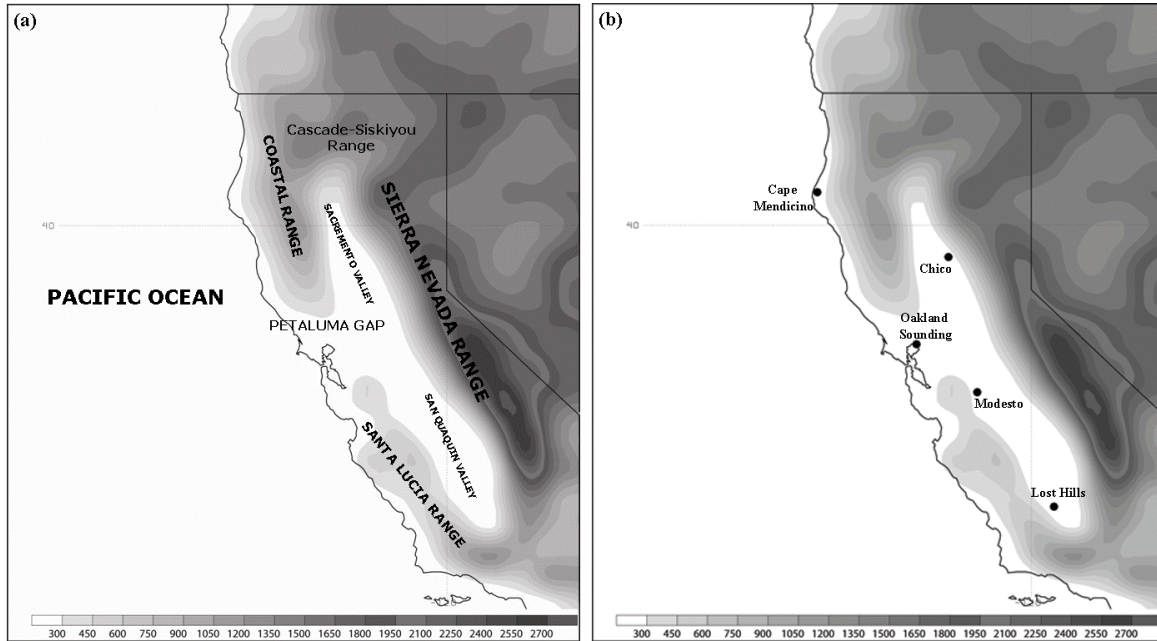
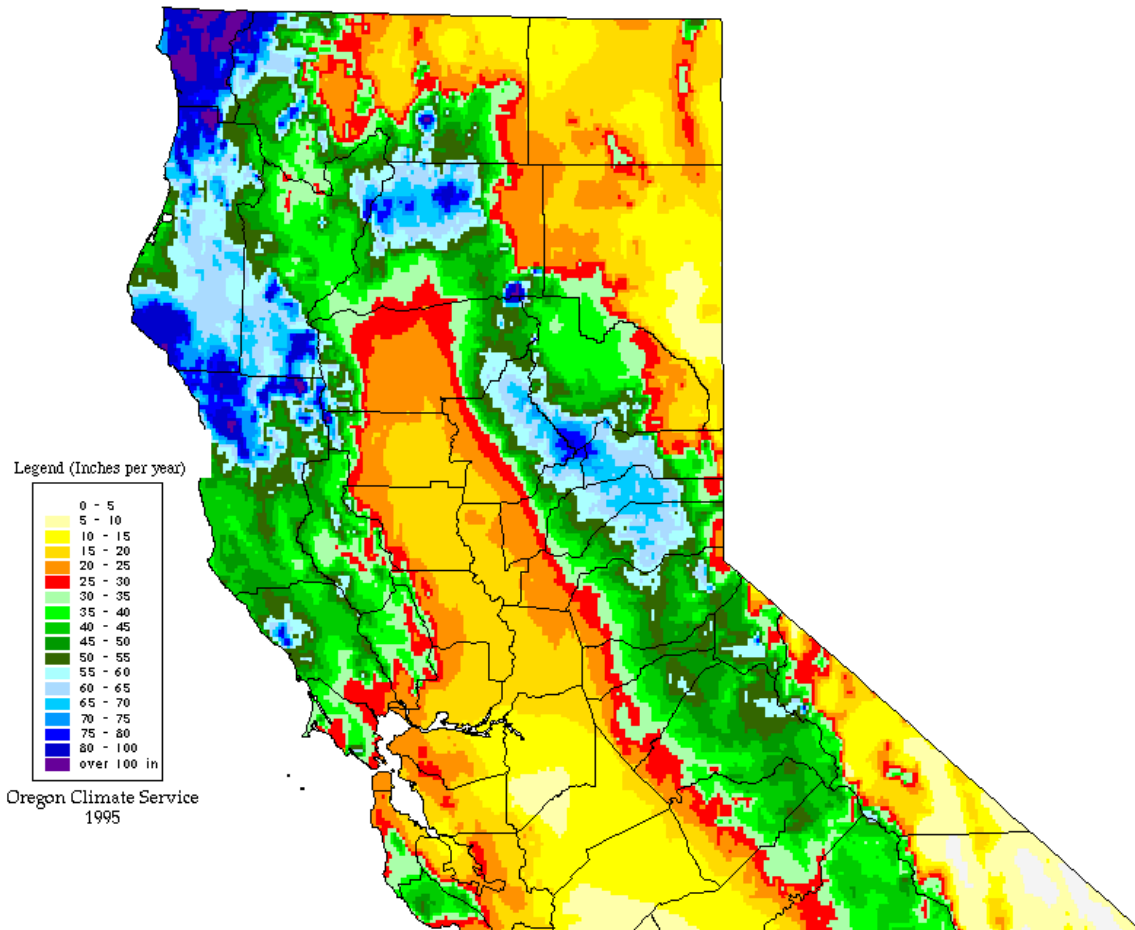


Figure 1: California terrain elevation with and overlay of (a) significant geographical locations referenced in the text and (b) GPS-IPW locations and the Oakland sounding site.



Annual Average Precipitation (Inches),
Northern California

Period: 1961-1990

Figure 2: Average annual rainfall for northern California from 1961-1990. (Source: Oregon Climate Service)

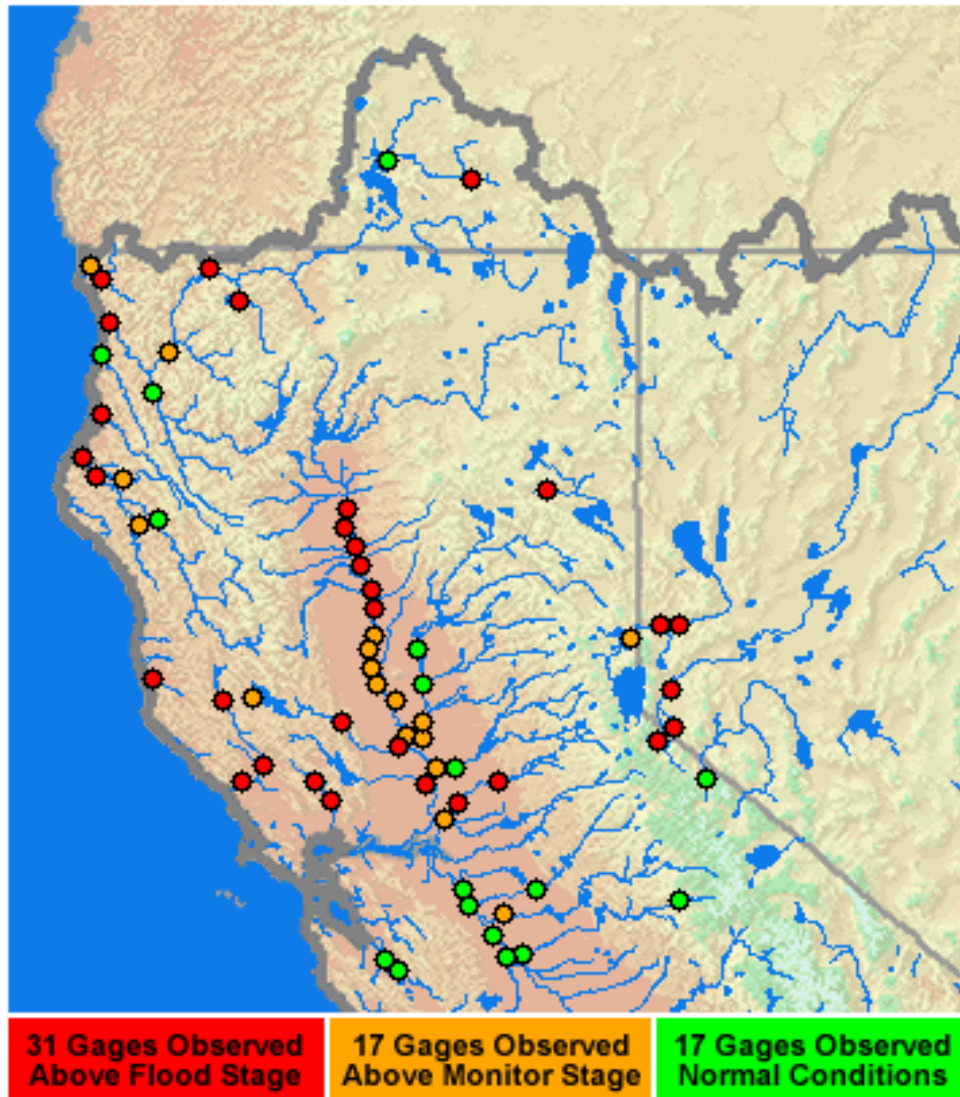


Figure 3: Highest river flood stage observed from December 24, 2005 to January 7, 2006.
Source: California Nevada River Forecast Center.

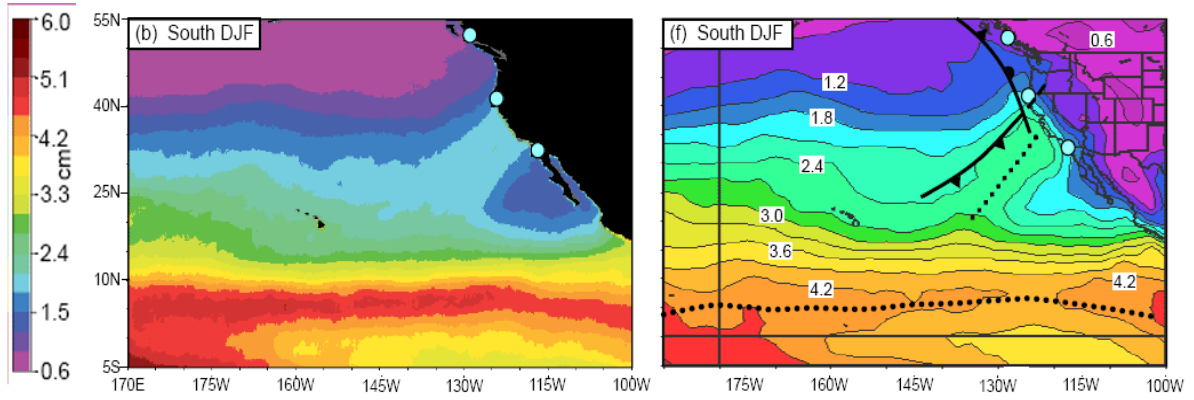


Figure 4: Composite SSM/I IWV (left) and NCEP reanalysis IWV and fronts (right) of winter atmospheric river cases making landfall on California coast (from Neiman et al. 2007). Units of IWV in cm.

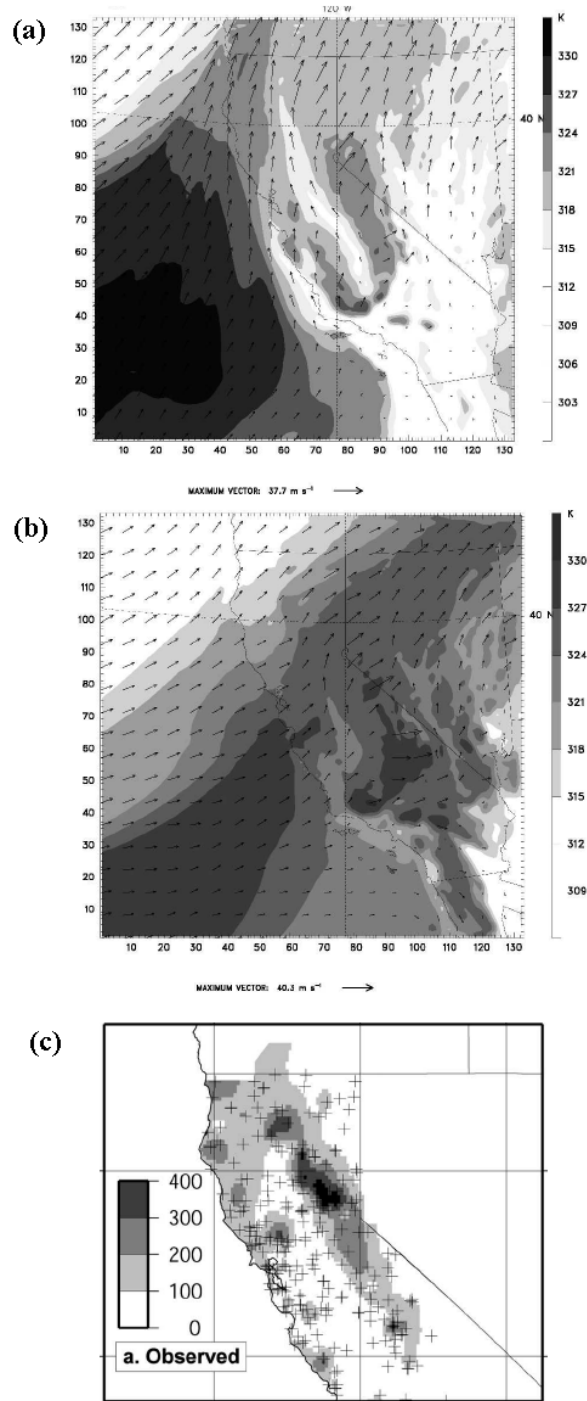


Figure 5: Fifth Generation Pennsylvania State University-UCAR Mesoscale Model (MM5) low-level (their σ level 0.95) winds (arrows in m s^{-1}) and θ_e (shaded in K) from Galewsky and Sobel (2005) for the New Year's Day flood of 1996 for (a) 31 Dec. 1996, and (b) 1 Jan. 1997; (c) Observed precipitation (mm) from 00 UTC 31 Dec., 1996 – 00 UTC 4 Jan., 1997.

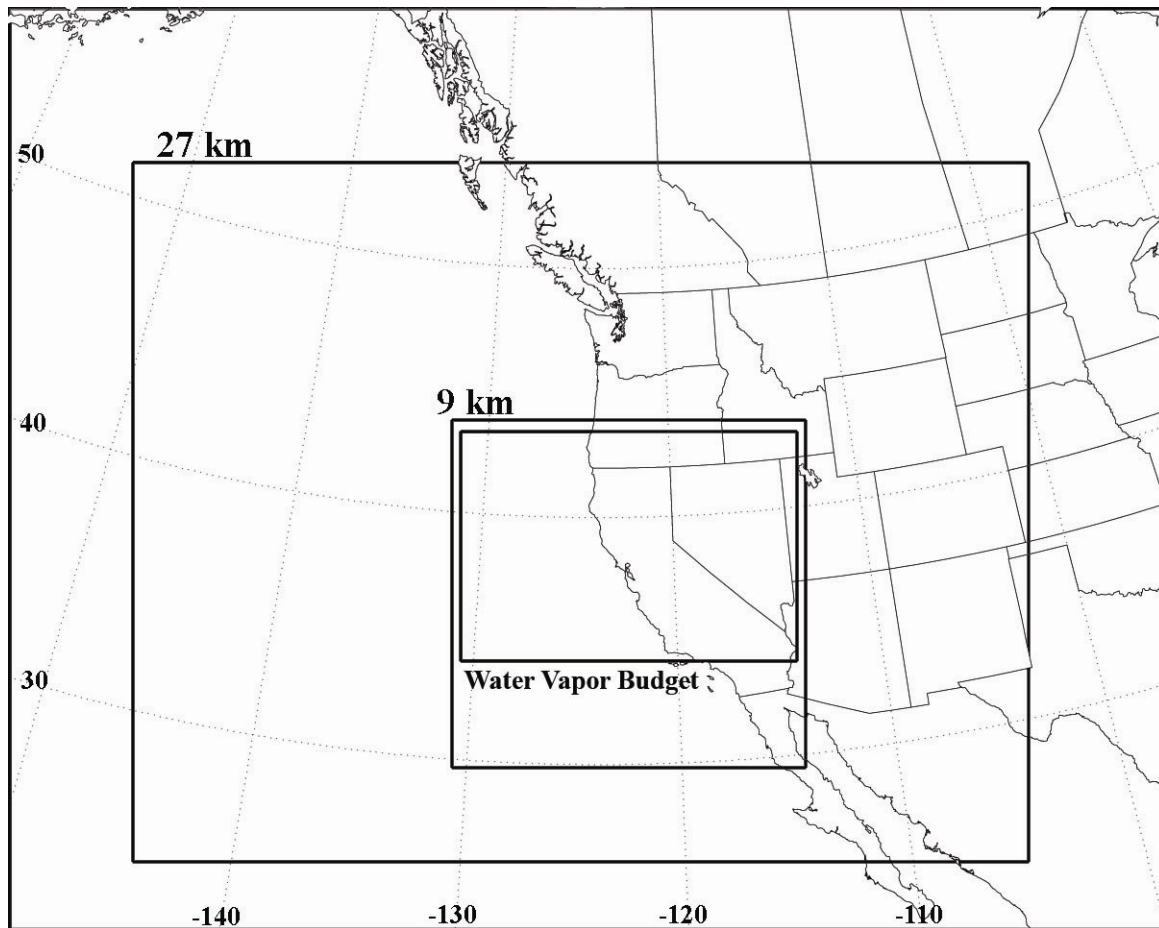


Figure 6: WRF model domain set up for 27 km outer and 9 km inner domains, and the large scale water vapor budget domain within the inner model domain.

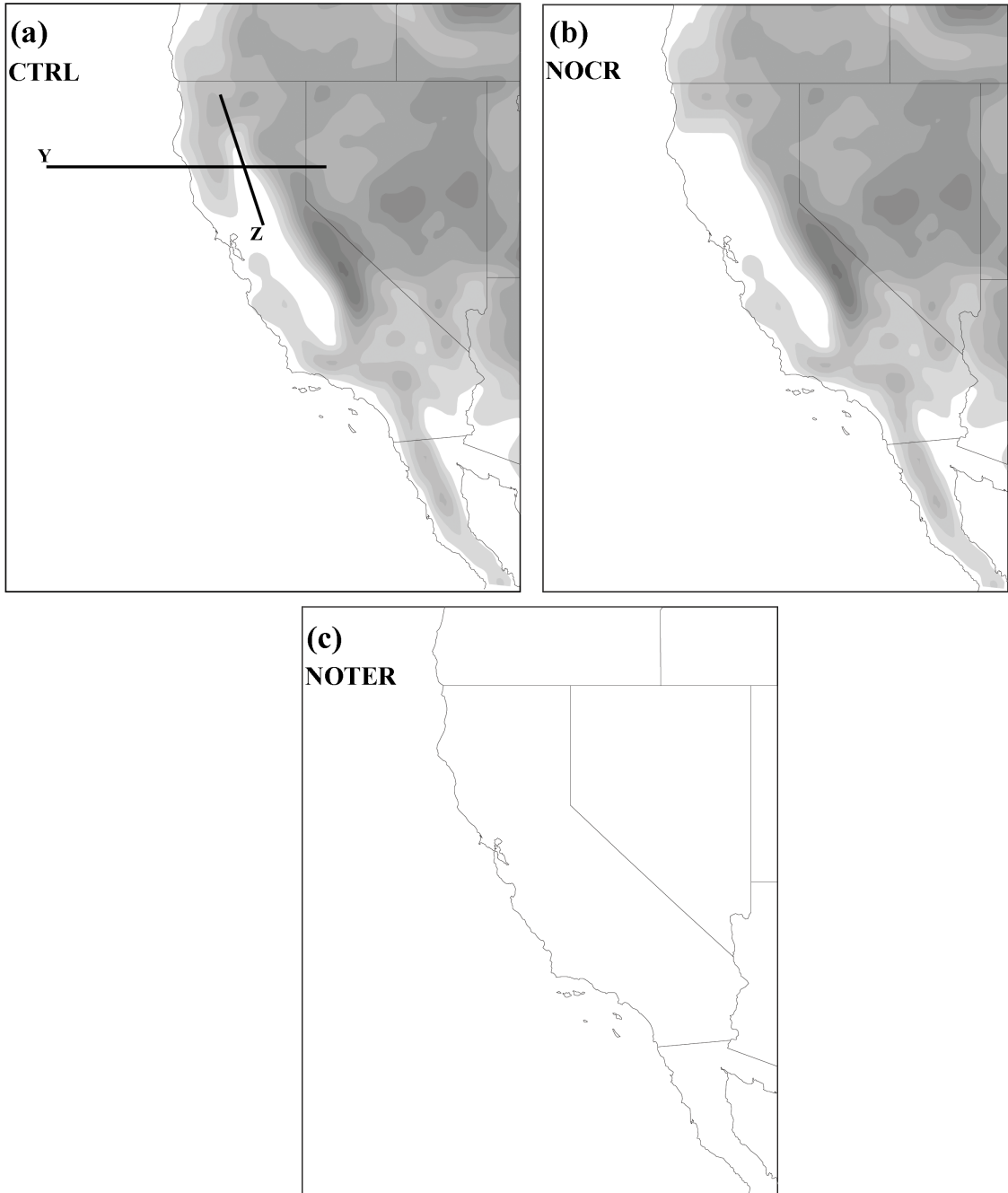


Figure 7: WRF model terrain elevation (shaded) for (a) CTRL, (b) NOCR, and (c) NOTER runs (each labeled), and cross section reference lines labeled Y and Z.

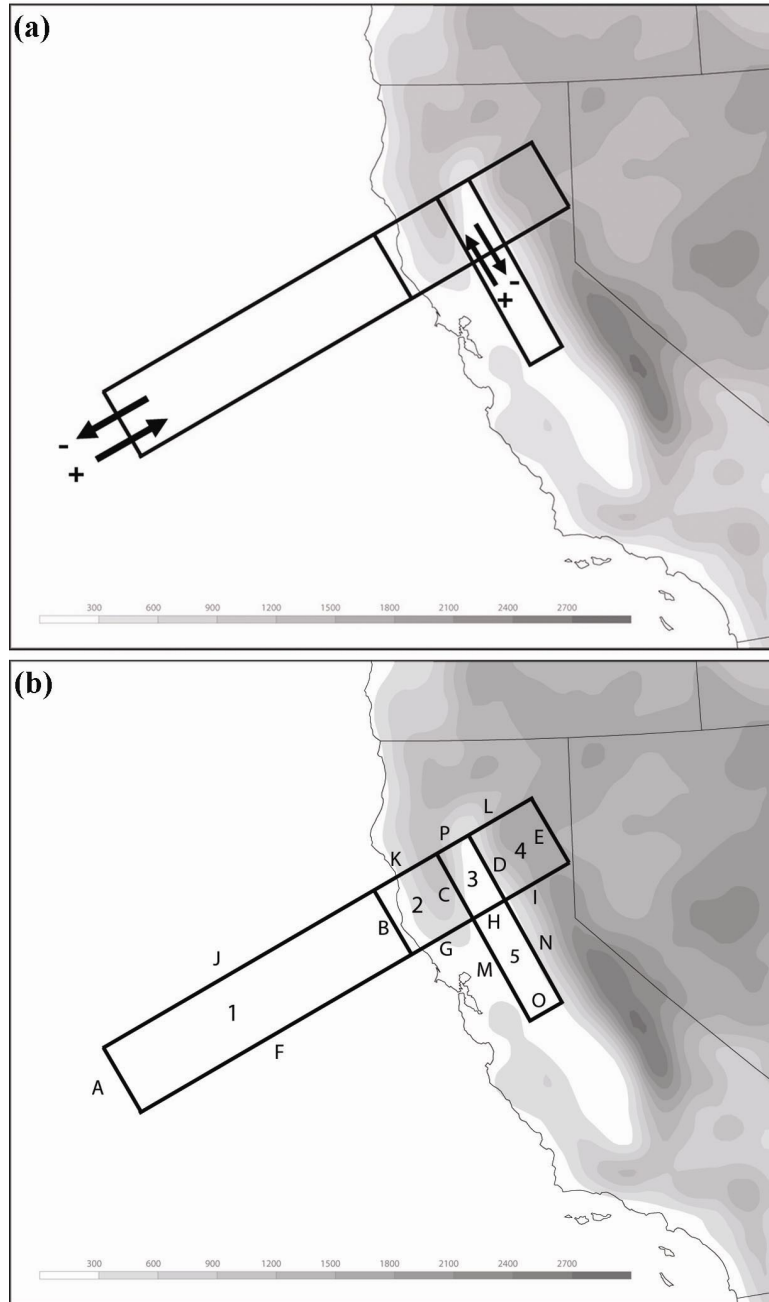


Figure 8: WRF model terrain (shaded in m) with (a) the assignment of positive and negative flux values used in the moisture flux analysis of box sides (the same convention applies to each box side), and (b) layout of small scale moisture budget boxes with sides labeled A-P and boxes labeled 1-5. Note: sign conventions here are not the same as those used in the moisture budget.

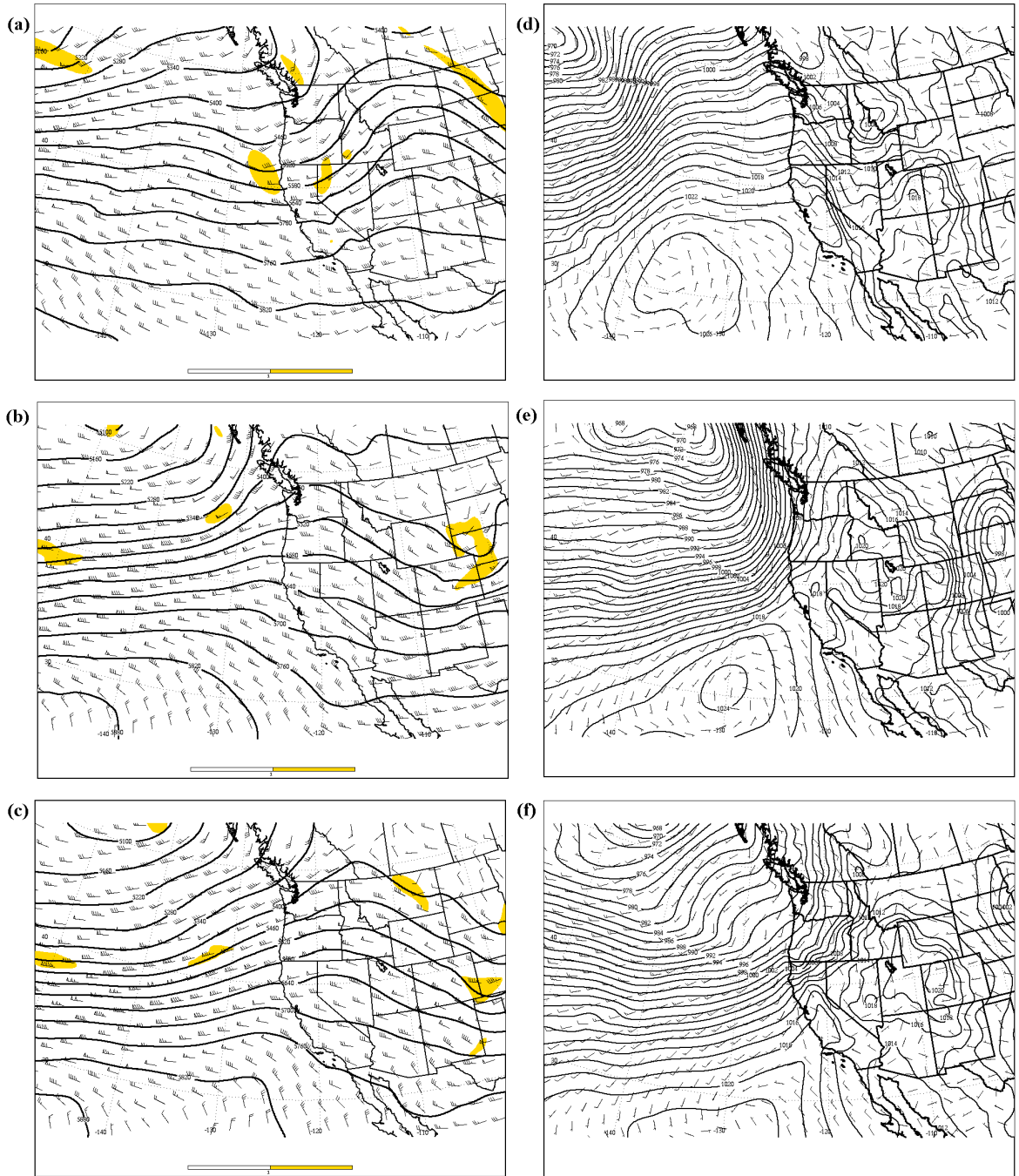


Figure 9: NARR 500 mb geopotential height (contours in m), vorticity (shaded in 10^4 s^{-1}), and wind (barbs) for (a) 00 UTC 29 December, (b) 00 UTC 30 December, and c) 12 UTC 30 December. NARR sea-level pressure (contours in mb) and 10-m wind (barbs) for, (d) 00 UTC 29 December, (e) 00 UTC 30 December, and (f) 12 UTC 30 December. All winds in knots.

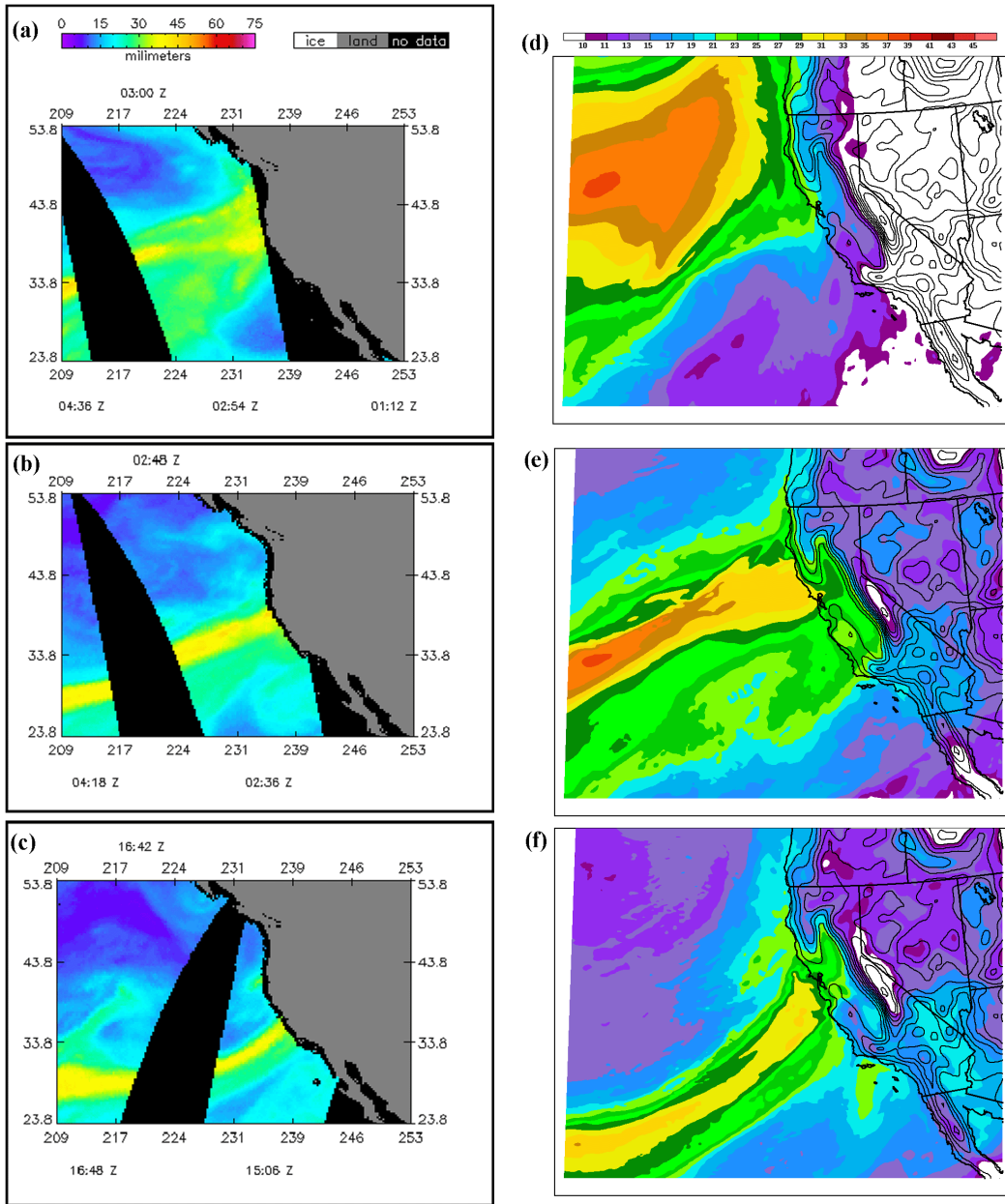


Figure 10: SSM/I passes of IWPV (mm) from (a) 03 UTC 30 December, 2005, (b) 03 UTC 31 December, 2005, and (c) 15 UTC 31 December, 2005. Corresponding WRF simulated IWPV (mm) from CTRL run for (d) 03 UTC 30 December, 2005, (e) 03 UTC 31 December, 2005, and (f) 15 UTC 31 December, 2005. Dark regions are areas not covered by ascending and descending satellite passes. Source: Remote Sensing Systems SSM/I data.

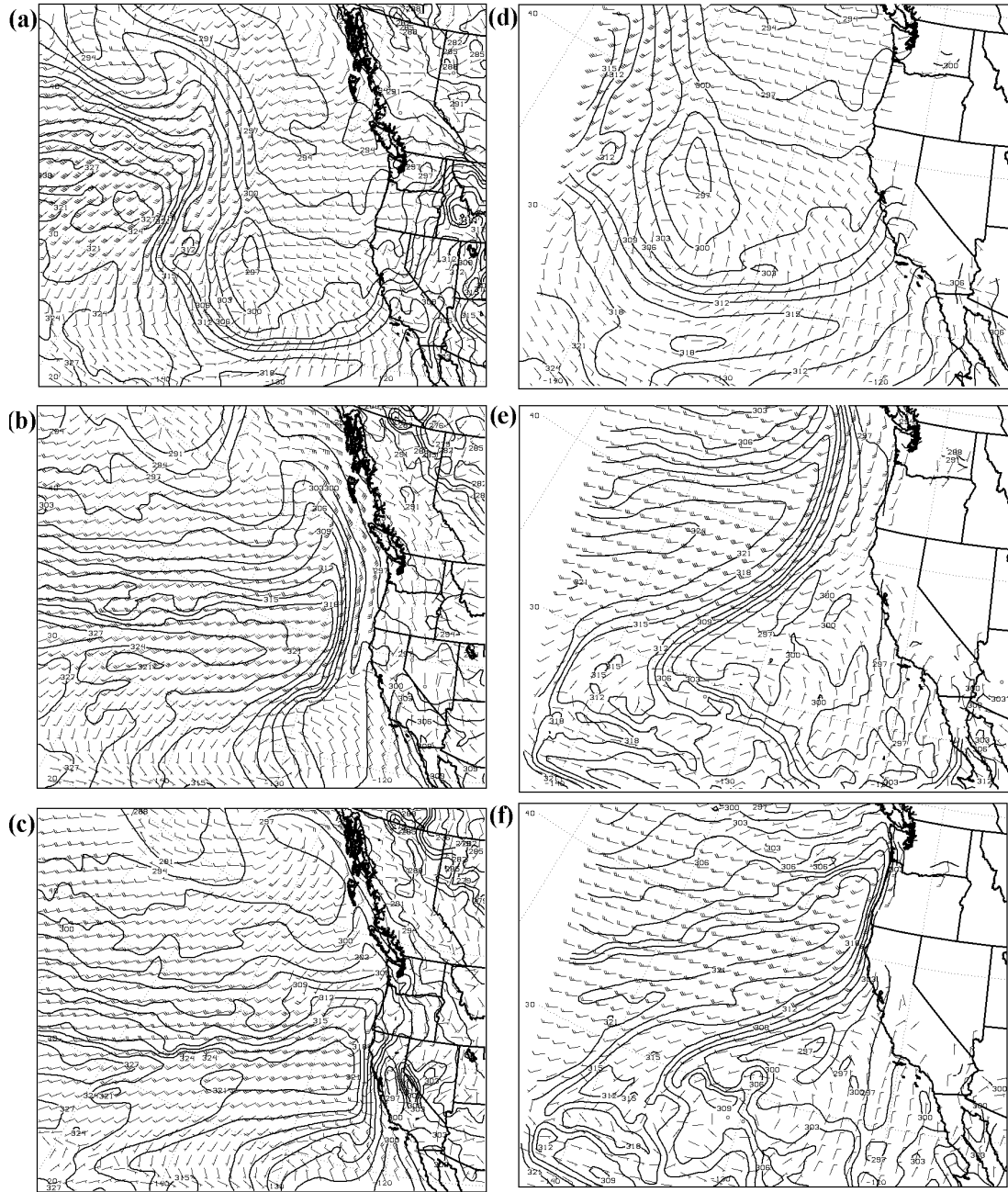


Figure 11: NARR 925 mb equivalent potential temperature (contours in K) and wind (barbs in knots) at (a) 00 UTC 29 December, (b) 00 UTC 30 December, and (c) 12 UTC 30 December. (d), (e), and (f) for the same times but for the WRF CTRL simulation.

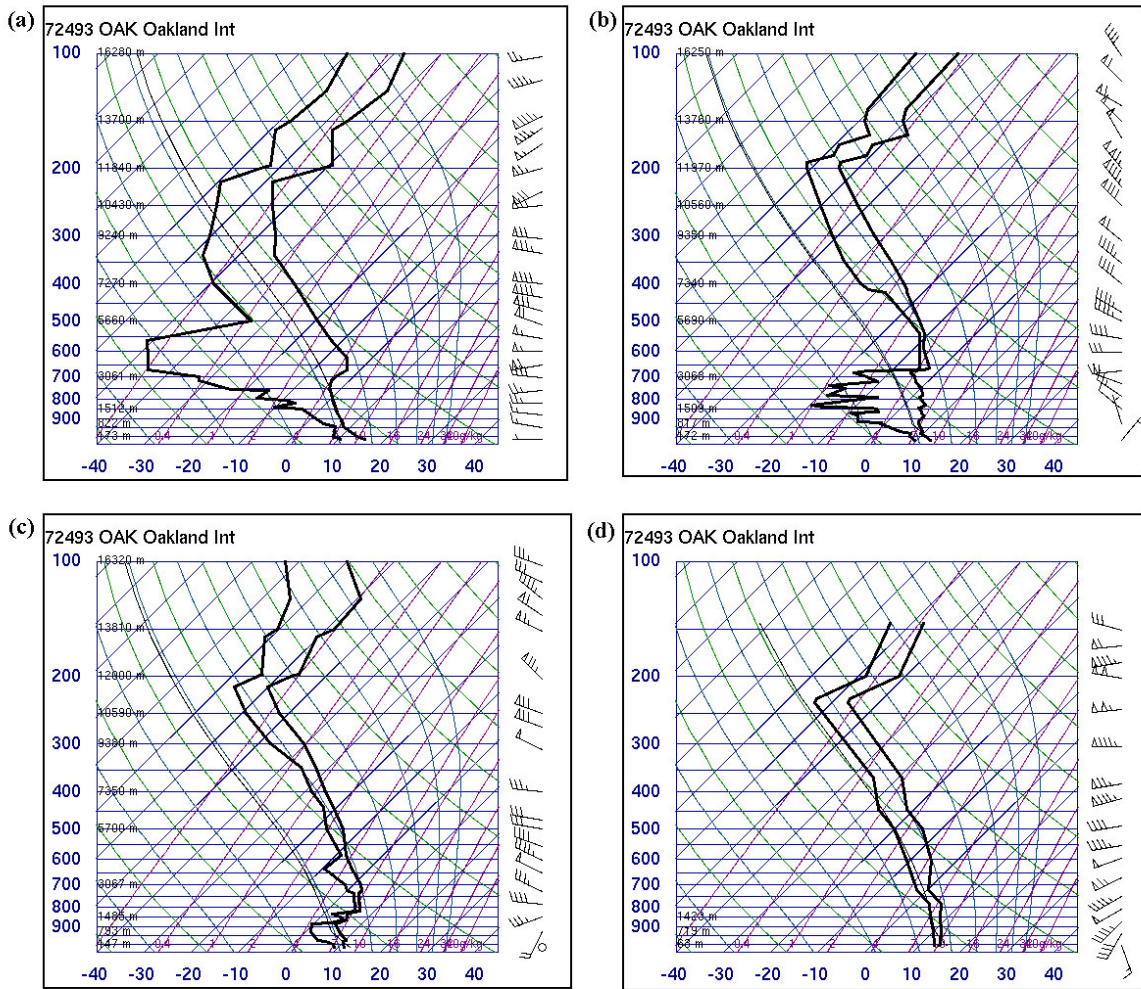


Figure 12: Upper air sounding from Oakland, CA at (a) 00 UTC 29 December, (b) 00 UTC 30 December, (c) 12 UTC 30 December, and (d) 09 UTC 31 December.

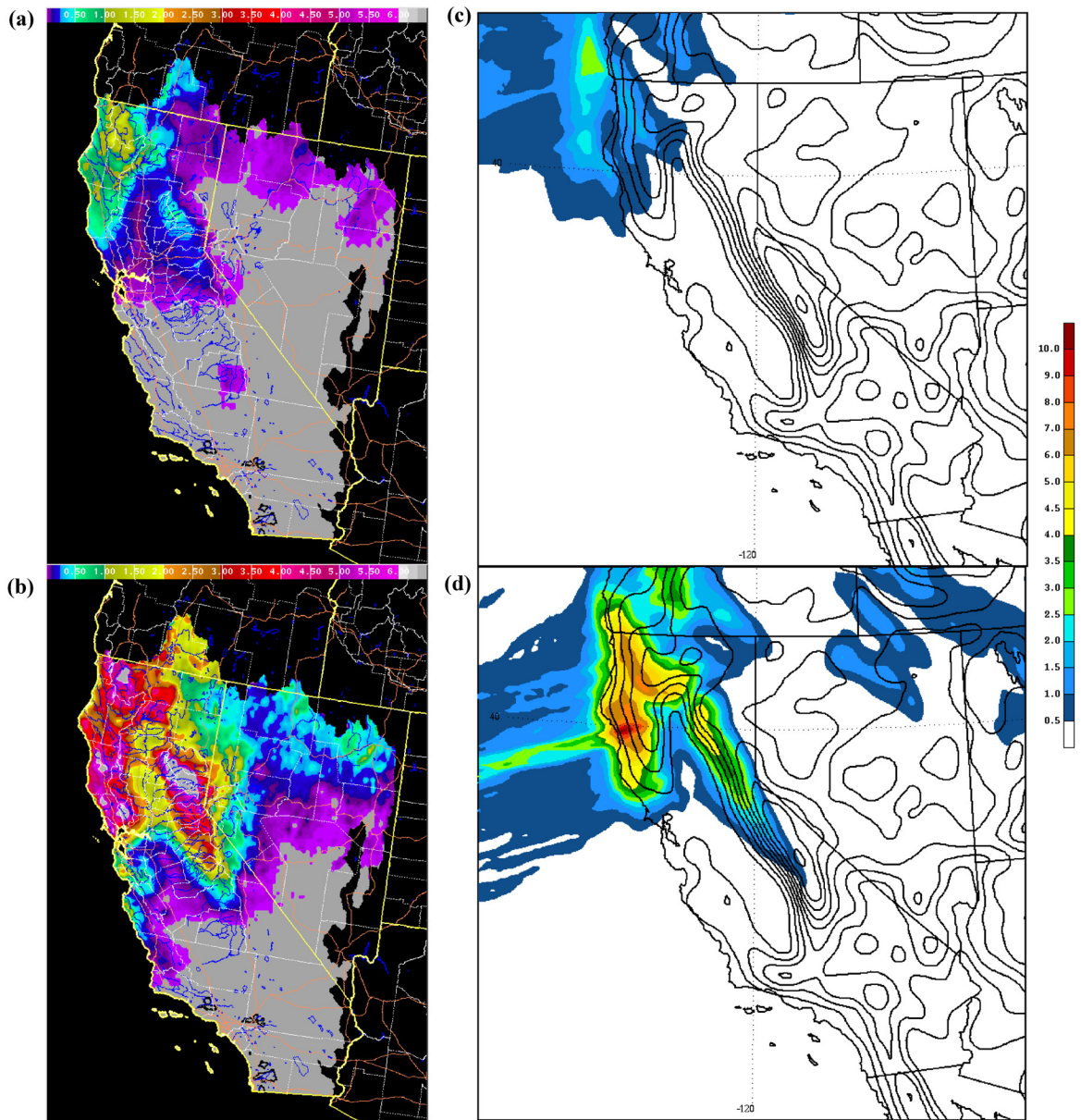


Figure 13: Gridded observed 24 hour precipitation (mm) for (a) 12 UTC 29 Dec. to 12 UTC 30 Dec., 2005 and (b) 12 UTC 30 Dec. to 12 UTC 31 Dec., 2005. WRF CTRL run 24 hour precipitation for (c) same period as (a), and (d) same period as (b). Source of gridded precipitation: California-Nevada River Forecast Center (CNRFC). Gridded analysis area ends at the CNRFC region borders.

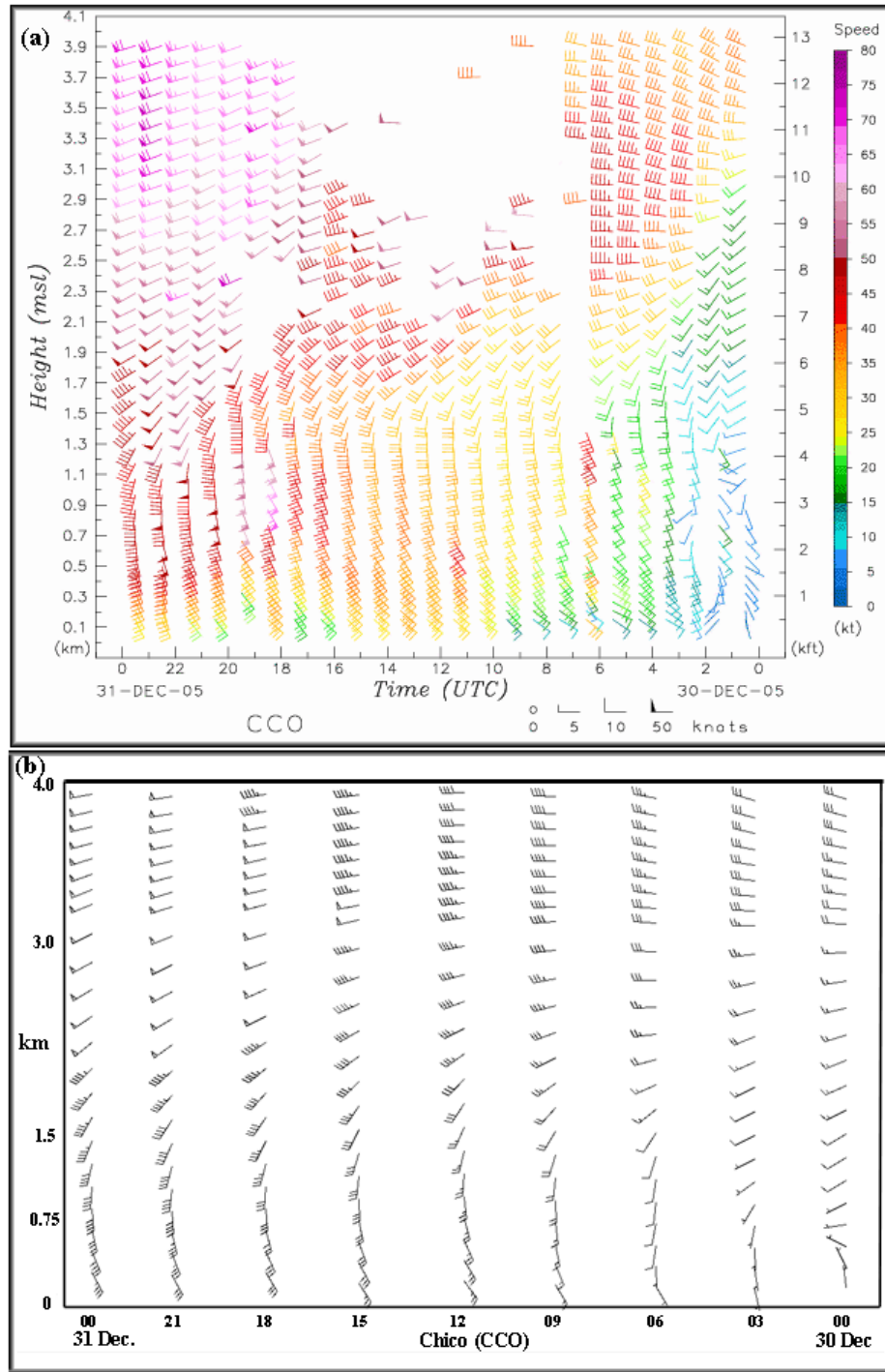


Figure 14: (a) Chico (CCO), CA wind profiler data for 30 Dec., 2005 up to 4 km. (b) WRF CTRL simulated winds below 600 mb at Chico, CA. Wind barbs are in knots, with time reading from right to left.

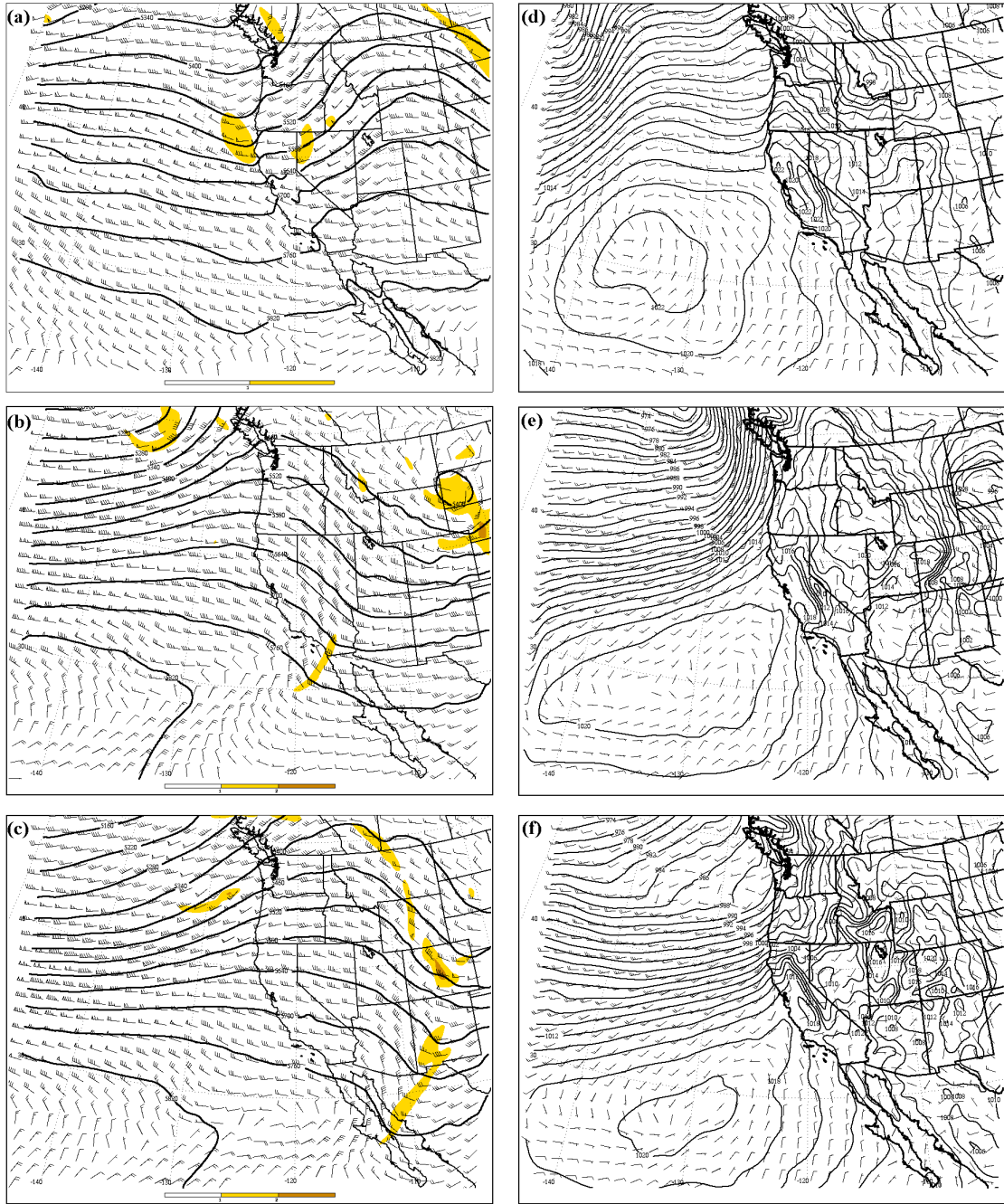


Figure 15: WRF CTRL run 500 mb geopotential heights (contours in m), vorticity (shaded in 10^4 s^{-1}) and wind (barbs in knots) at (a) 00 UTC 29 Dec., (b) 00 UTC 30 Dec., and (c) 12 UTC 30 Dec. WRF CTRL run sea-level pressure (contours in mb) and 10 m winds (barbs in m/s) at (d) 00 UTC 29 Dec., (e) 00 UTC 30 Dec., and (f) 12 UTC 30 Dec.

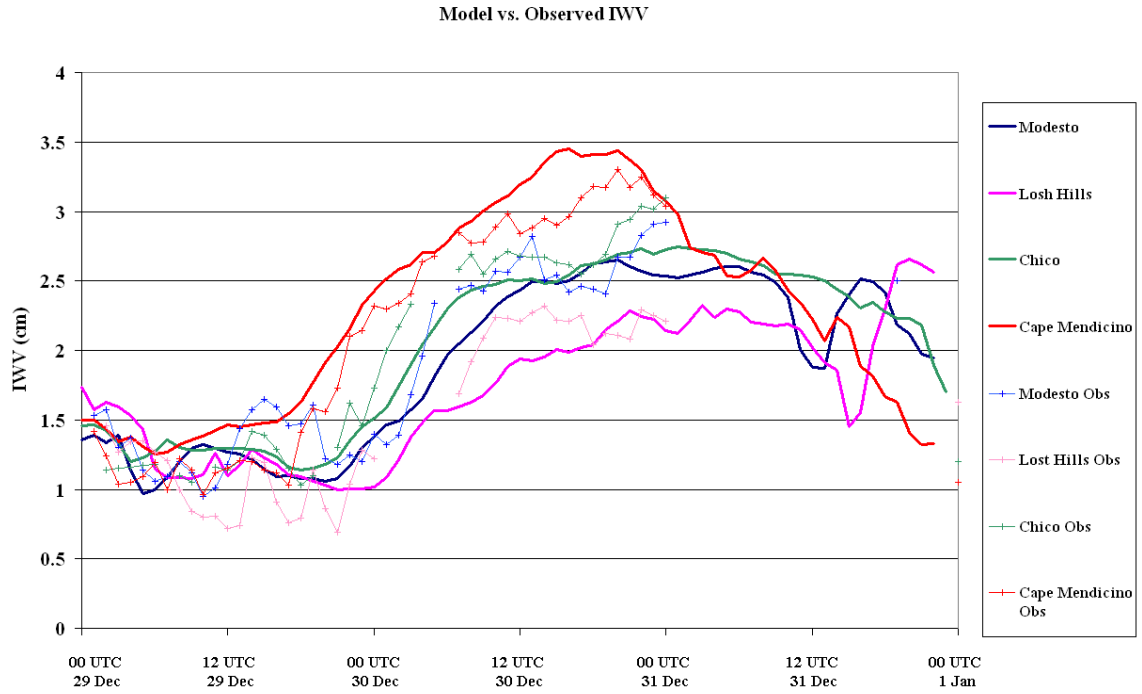


Figure 16: Comparison of GPS IVW (cm) values (cross-hatched lines) and WRF CTRL run simulated IWV values (solid lines in cm) at Cape Mendocino, Modesto, Chico, and Lost Hills.

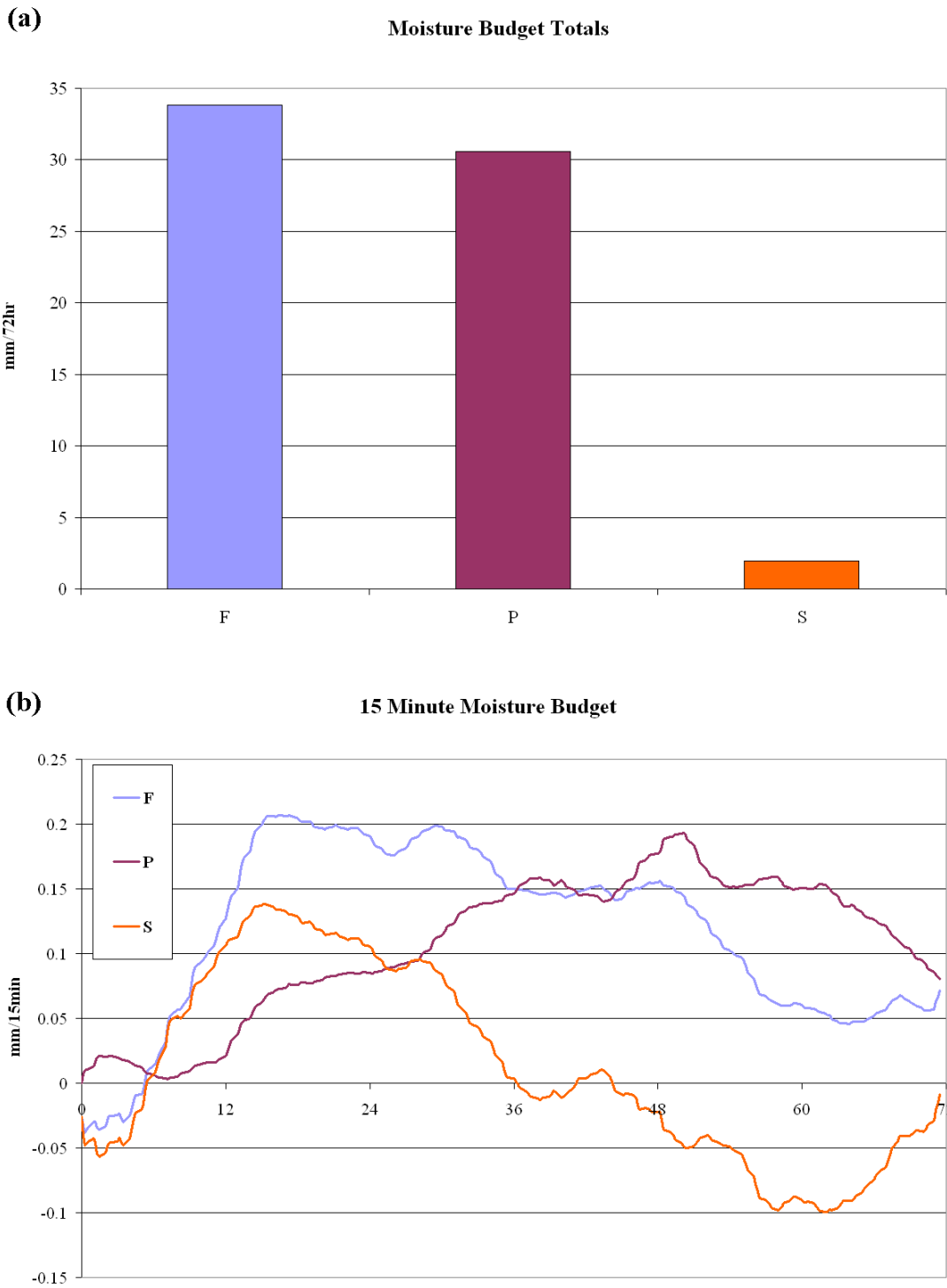


Figure 17 Large scale moisture budget of moisture flux convergence, precipitation, and storage for WRF CTRL run (a) 72 hour totals ($\text{mm } 72\text{hr}^{-1}$), and (b) 15 min rates ($\text{mm } 15\text{min}^{-1}$)

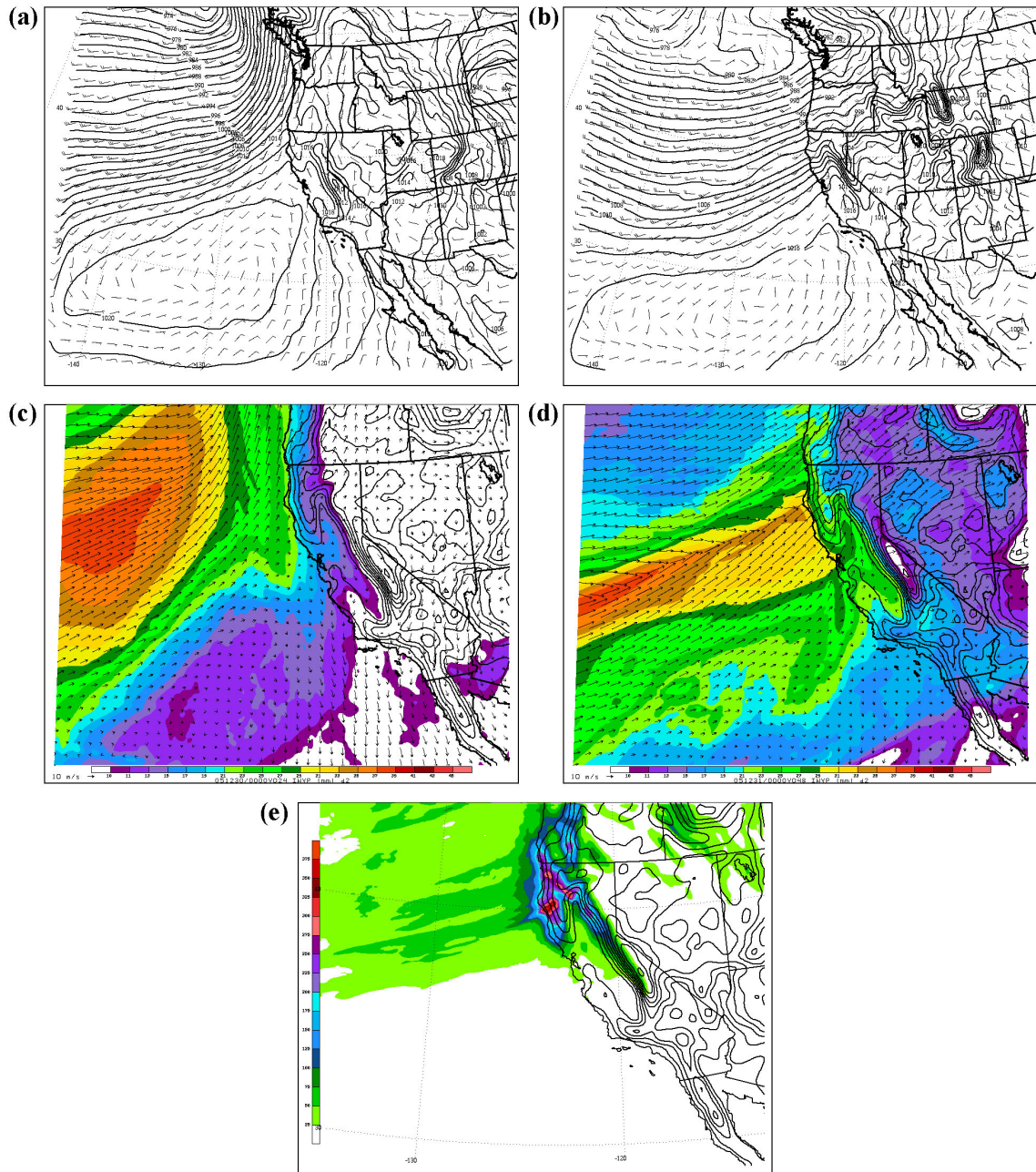


Figure 18: All plots from the WRF CTRL run: Sea-level pressure (contours in mb) and 10 meter winds (barbs in m s^{-1}) for (a) 00 UTC 30 Dec., and (b) 12 UTC 30 Dec., 2005. IWV (shaded) and $\sigma=0.9205$ winds (arrows in m s^{-1}) for (c) 00 UTC 30 Dec., and (d) 12 UTC 30 Dec. (e) 72 hour total precipitation (mm).

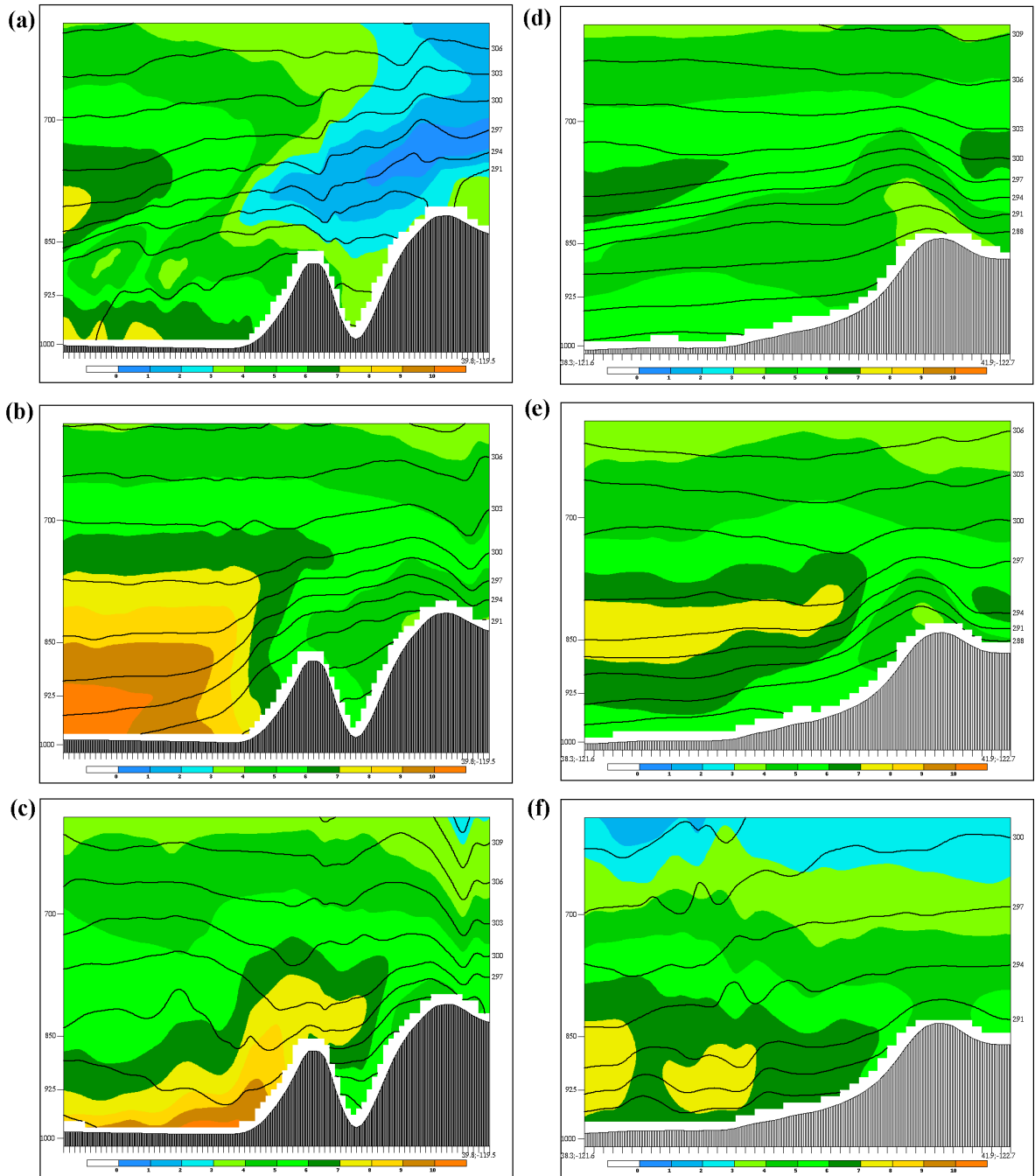


Figure 19: All figures are CTRL WRF cross-sections of potential temperature (contours in K) and water vapor mixing ratio (shaded in g kg^{-1}): for cross-section Y (see Fig. 7) (a) 00 UTC 30 Dec., (b) 12 UTC 30 Dec., and (c) 00 UTC 31 Dec., 2005; for cross-section Z (d) 12 UTC 30 Dec., (e) 00 UTC 31 Dec., and (f) 12 UTC 31 Dec.

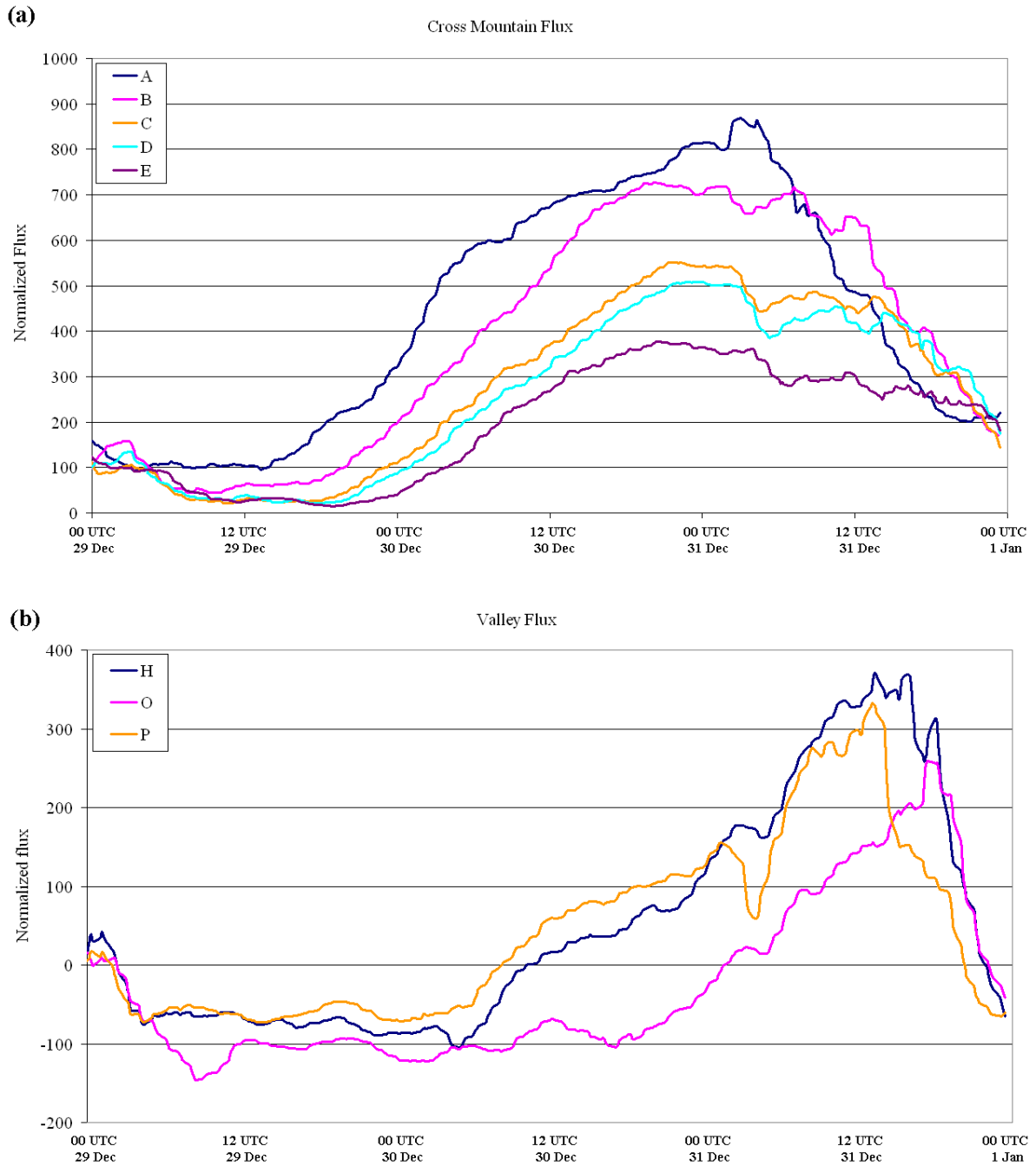


Figure 20: WRF CTRL time series of normalized moisture flux through sides (a) A-E (cross mountain flux), and (b) H, O, and P (valley flux). Flux values in $\text{kg m}^{-1} \text{s}^{-1}$.

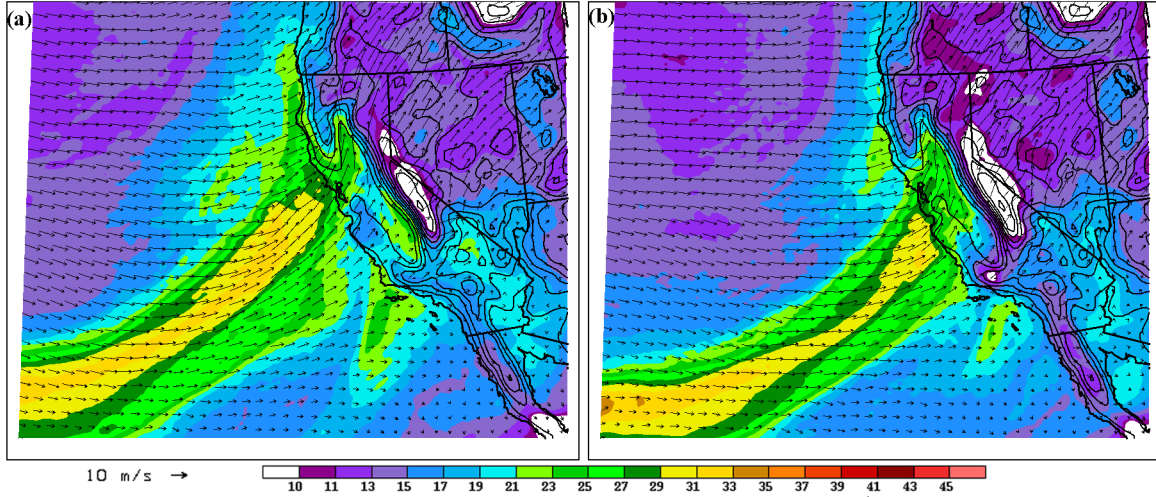


Figure 21: WRF CTRL run IWP (mm) and $\sigma=.9205$ winds ($m s^{-1}$) at (a) 13 UTC 31 Dec., and (b) 17 UTC 31 Dec.

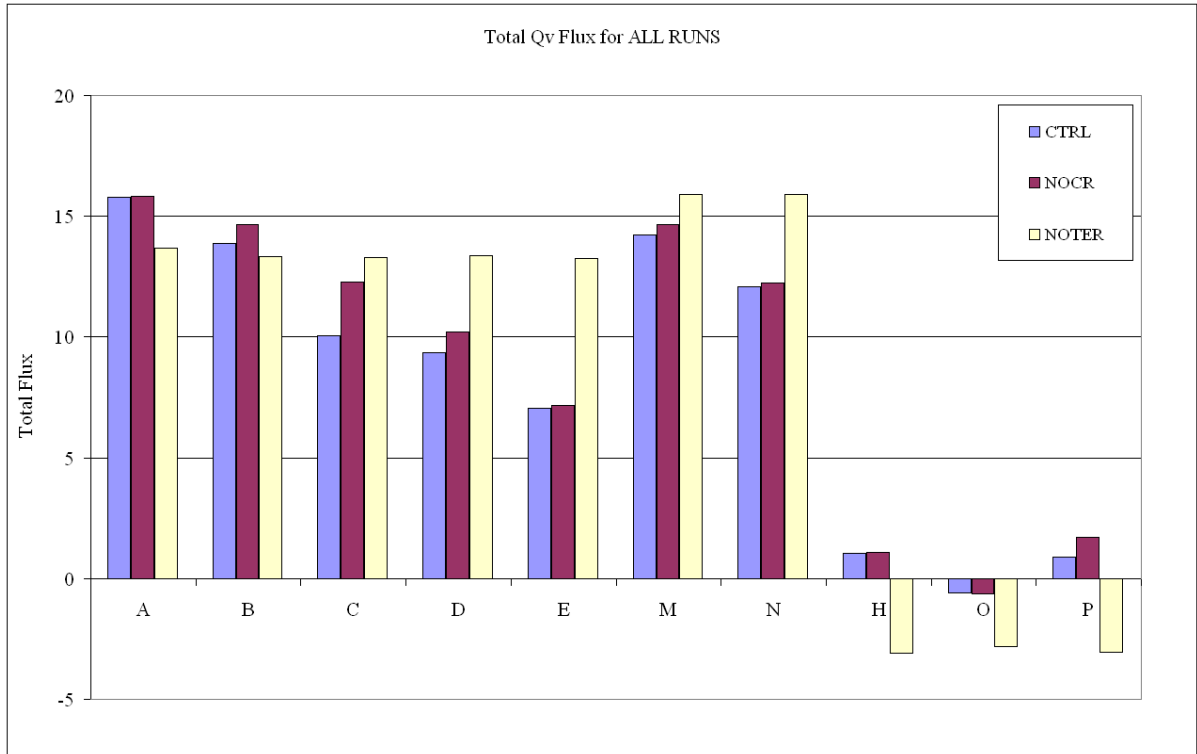


Figure 22: WRF 72 hour total water vapor flux ($\times 10^{12}$ kg 72hr^{-1}) through each box side (A-E, H, M, N, O, P) for the CTRL, NOCR, and NOTER runs.

Water Vapor Budget Totals

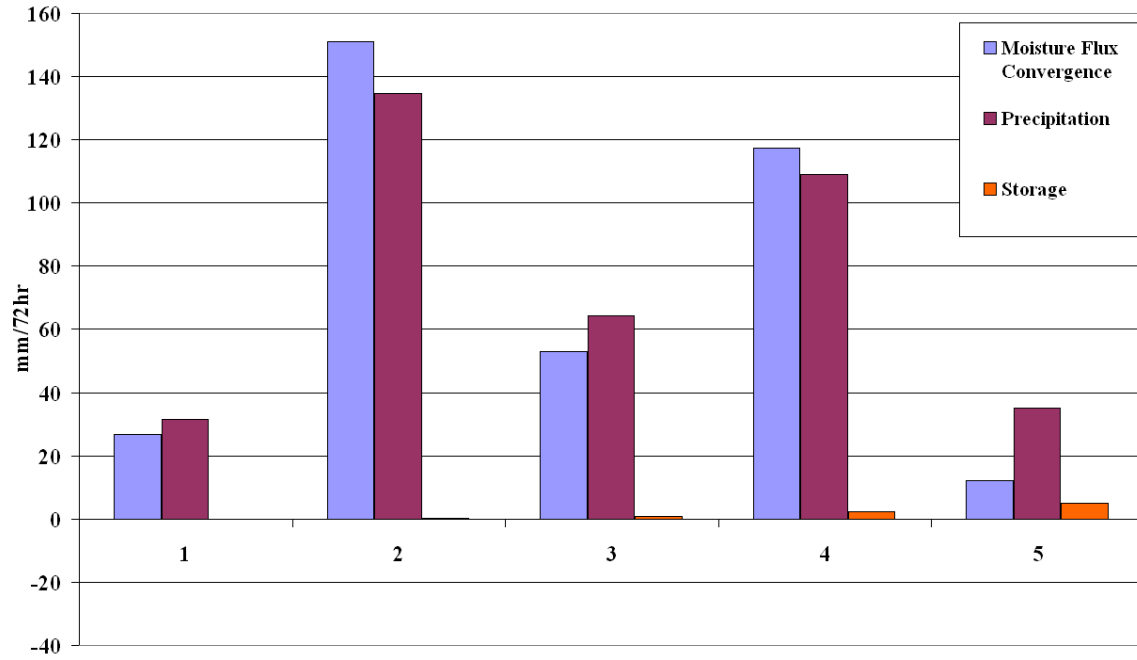


Figure 23: WRF CTRL run 72 hour moisture flux convergence, precipitation, and atmospheric storage. Units are $\text{mm } 72\text{hr}^{-1}$.

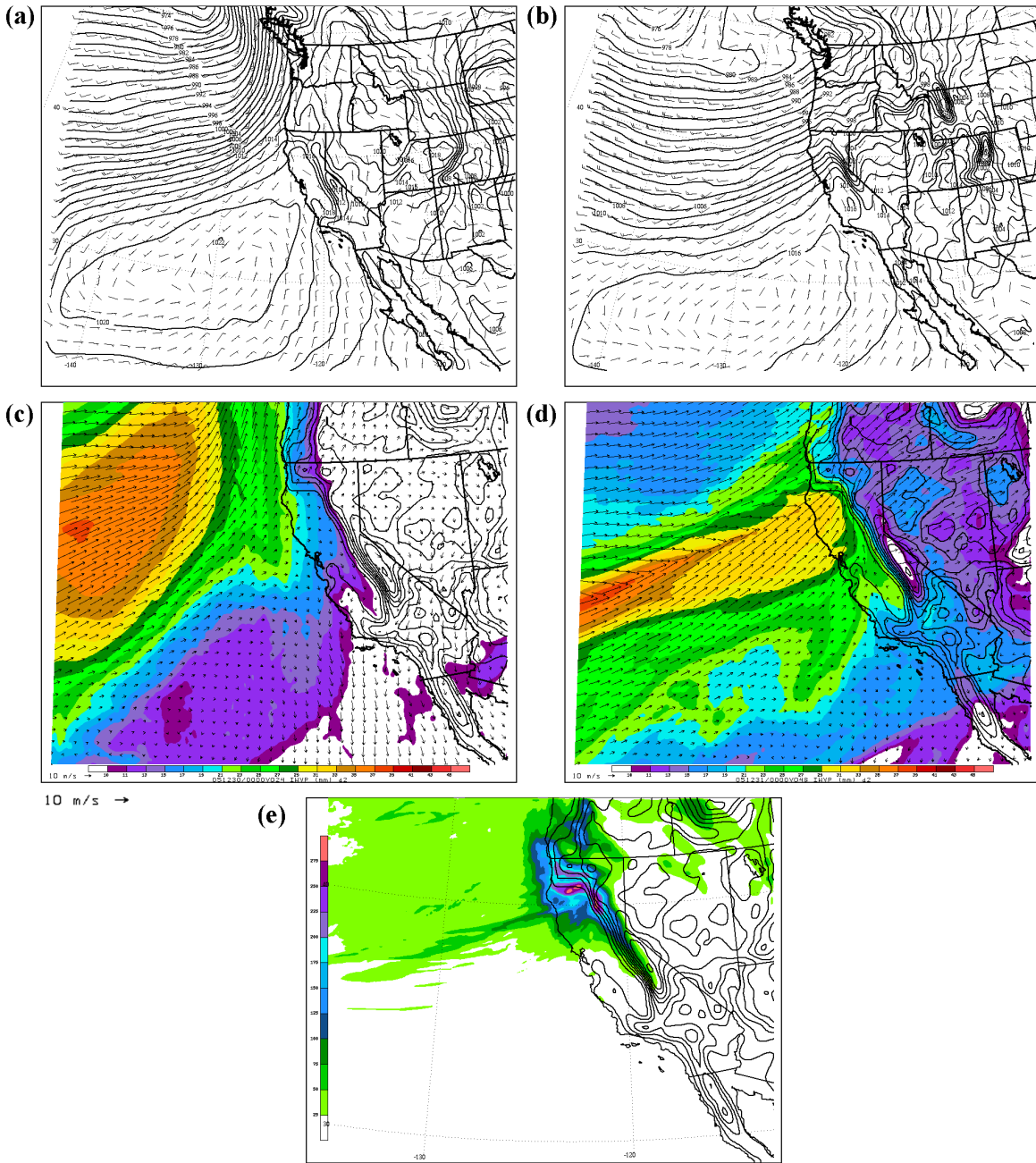


Figure 24: All plots from the WRF NOCR run: Sea-level pressure (contours in mb) and 10 meter winds (barbs in m s^{-1}) for (a) 00 UTC 30 Dec., and (b) 12 UTC 30 Dec., 2005. IWV (shaded in mm) and $\sigma=0.9205$ winds (arrows in m s^{-1}) for (c) 00 UTC 30 Dec., and (d) 12 UTC 30 Dec. (e) 72 hour total precipitation (mm).

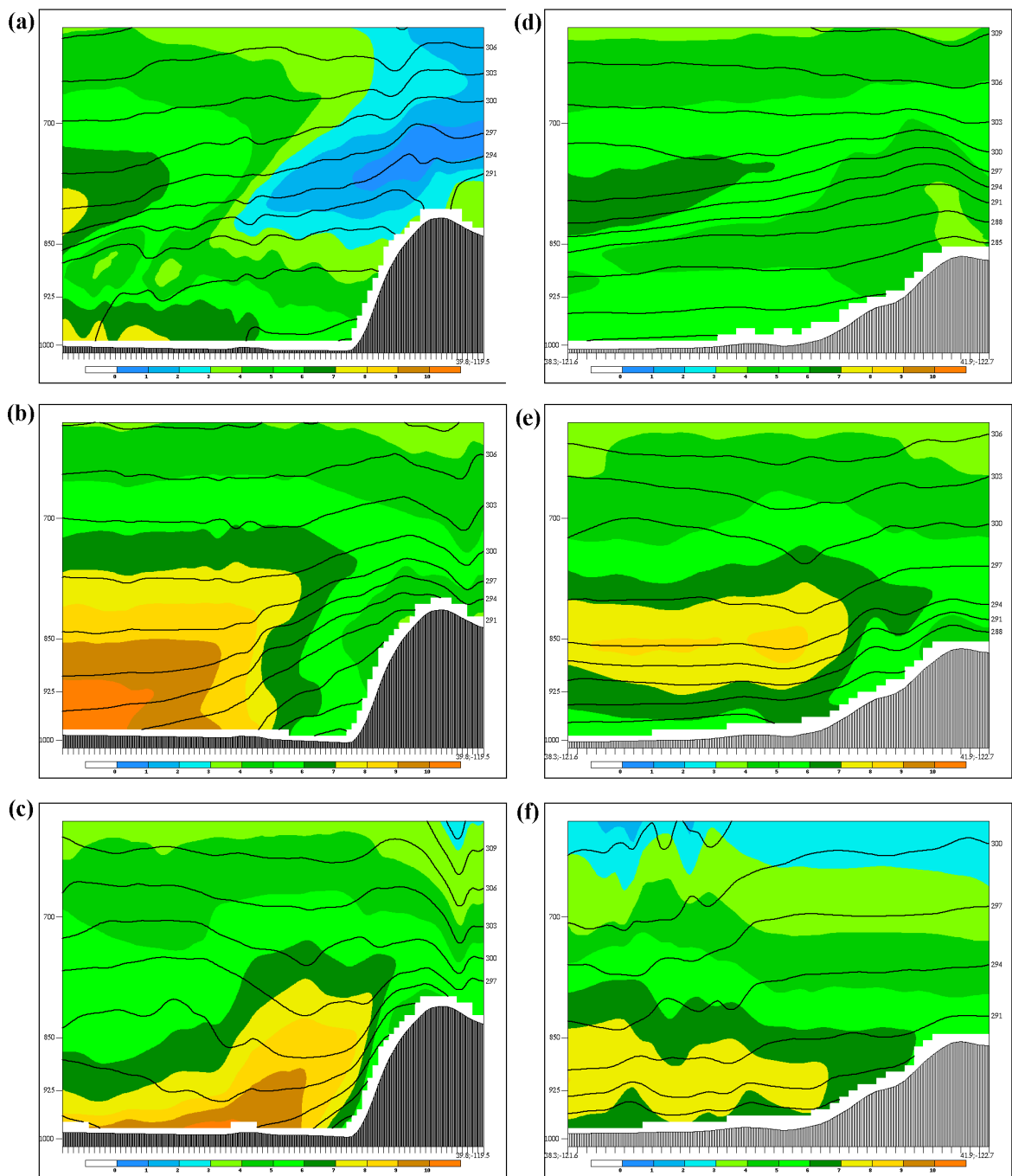


Figure 25: All figures are NOCR WRF cross-sections of potential temperature (contours in K) and water vapor mixing ratio (shaded in g kg^{-1}): for cross-section Y (see Fig. 7) (a) 00 UTC 30 Dec., (b) 12 UTC 30 Dec., and (c) 00 UTC 31 Dec., 2005; for cross-section Z (d) 12 UTC 30 Dec., (e) 00 UTC 31 Dec., and (f) 12 UTC 31 Dec.

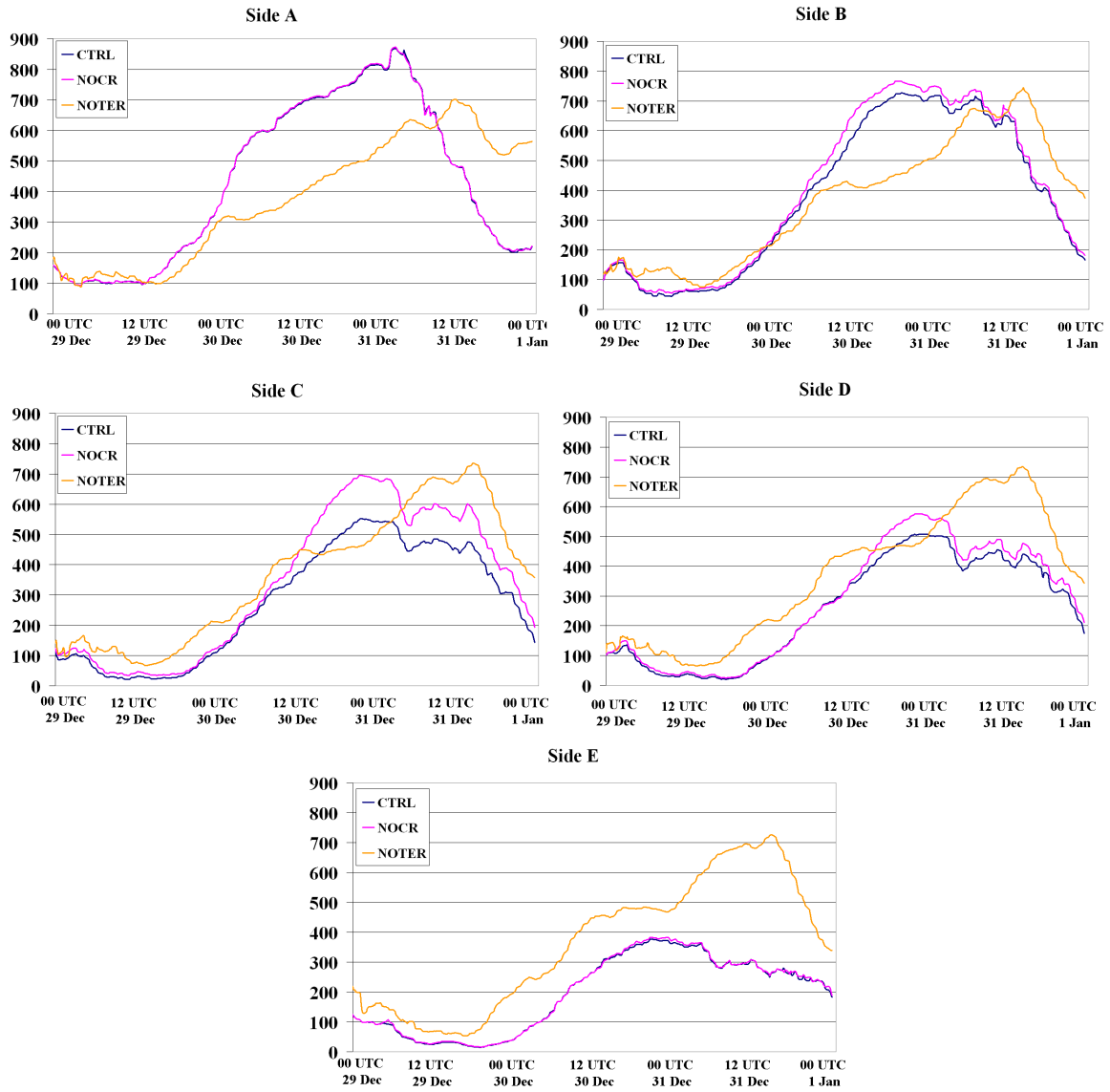


Figure 26: Comparison of normalized cross-mountain moisture flux through box sides A, B, C, D, and E for the CTRL, NOCR, and NOTER runs. Flux values in $\text{kg m}^{-1} \text{s}^{-1}$.

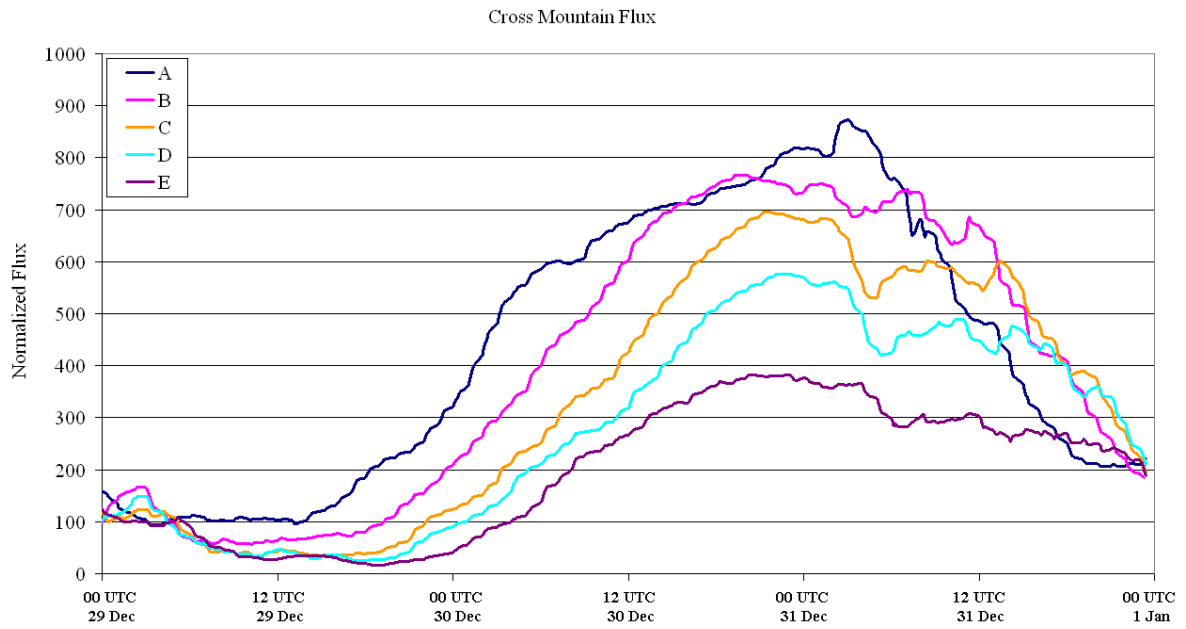


Figure 27: NOCR time series of normalized cross-mountain moisture flux through sides A-E. Flux values in $\text{kg m}^{-1} \text{s}^{-1}$.

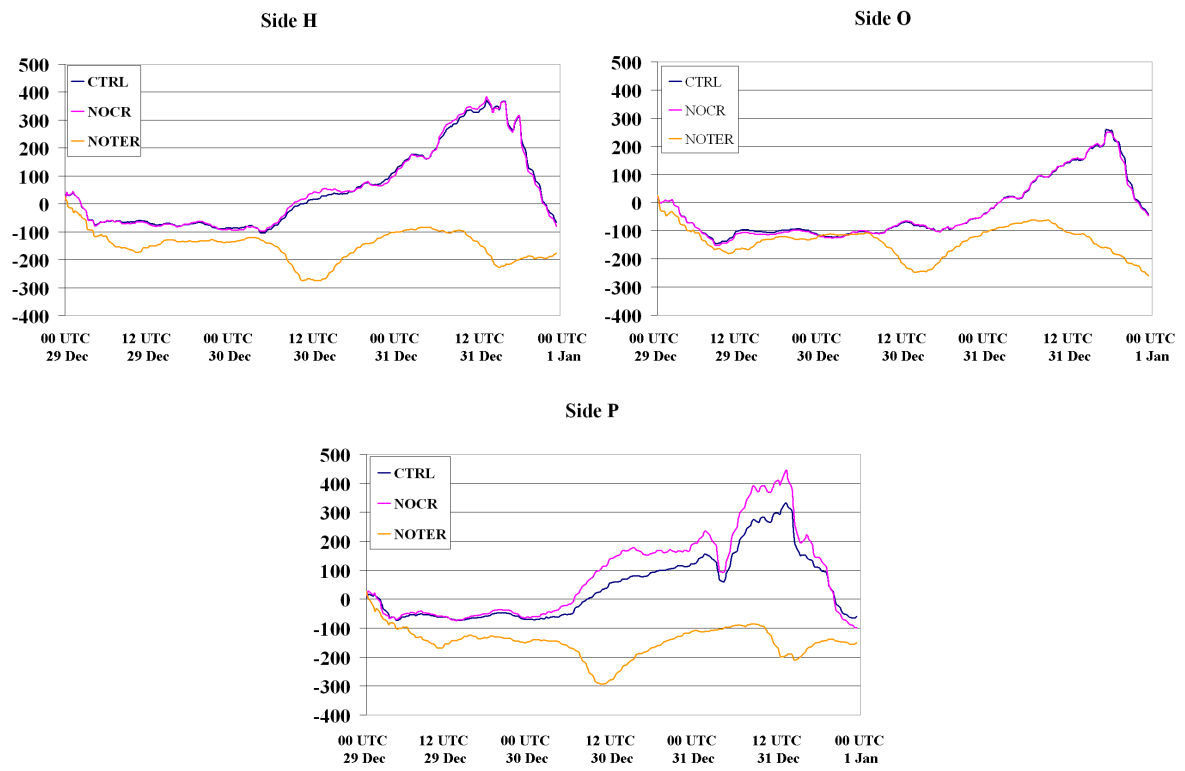


Figure 28: Comparison of normalized moisture flux through box sides H, O, and P for the CTRL, NOCR, and NOTER runs. Flux values in $\text{kg m}^{-1} \text{s}^{-1}$.

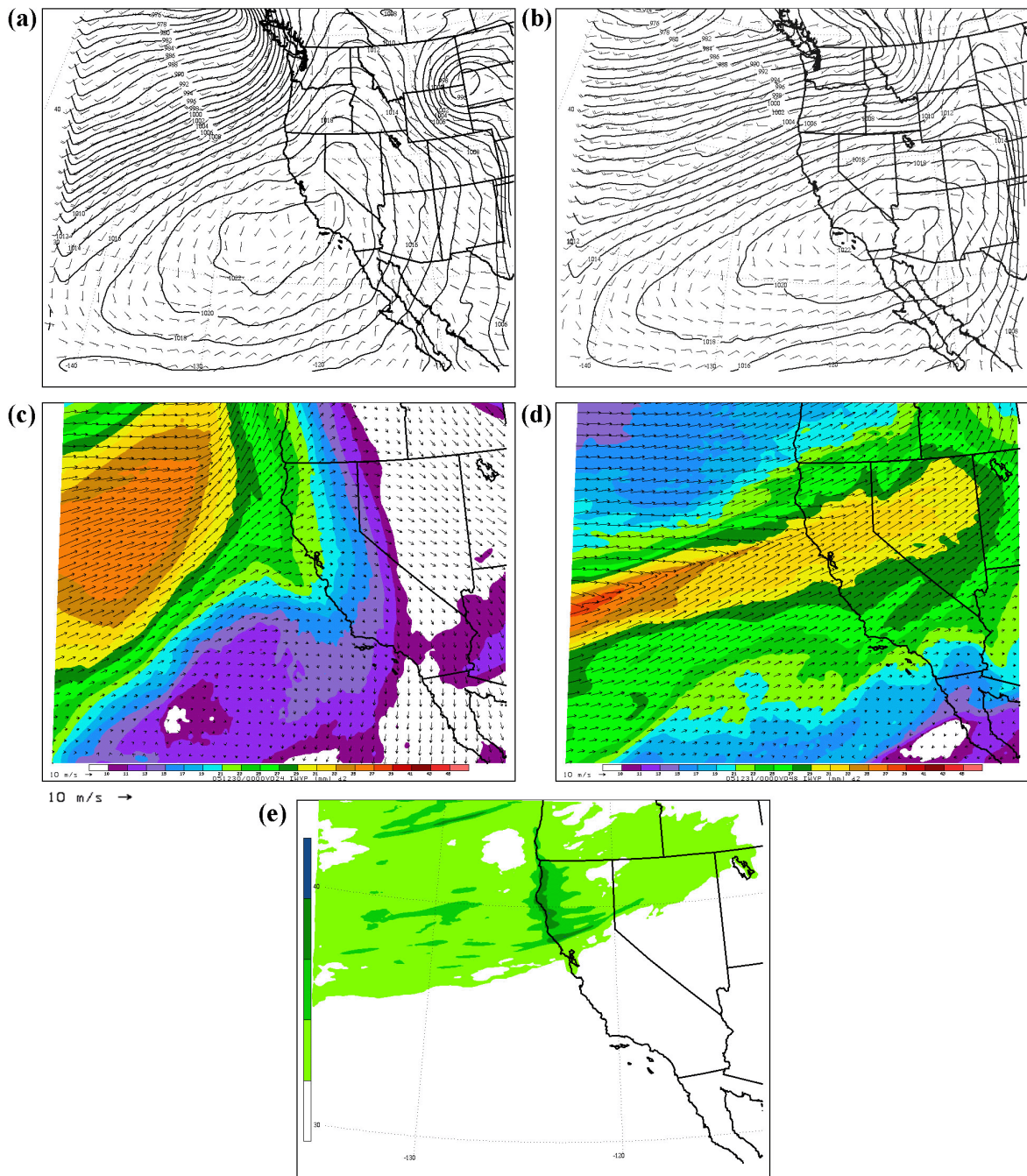


Figure 29: All plots from the WRF NOTER run: Sea-level pressure (contours in mb) and 10 meter winds (barbs in m s^{-1}) for (a) 00 UTC 30 Dec., and (b) 12 UTC 30 Dec., 2005. IWV (shaded in mm) and $\sigma=.9205$ winds (arrows in m s^{-1}) for (c) 00 UTC 30 Dec., and (d) 12 UTC 30 Dec. (e) 72 hour total precipitation (mm).

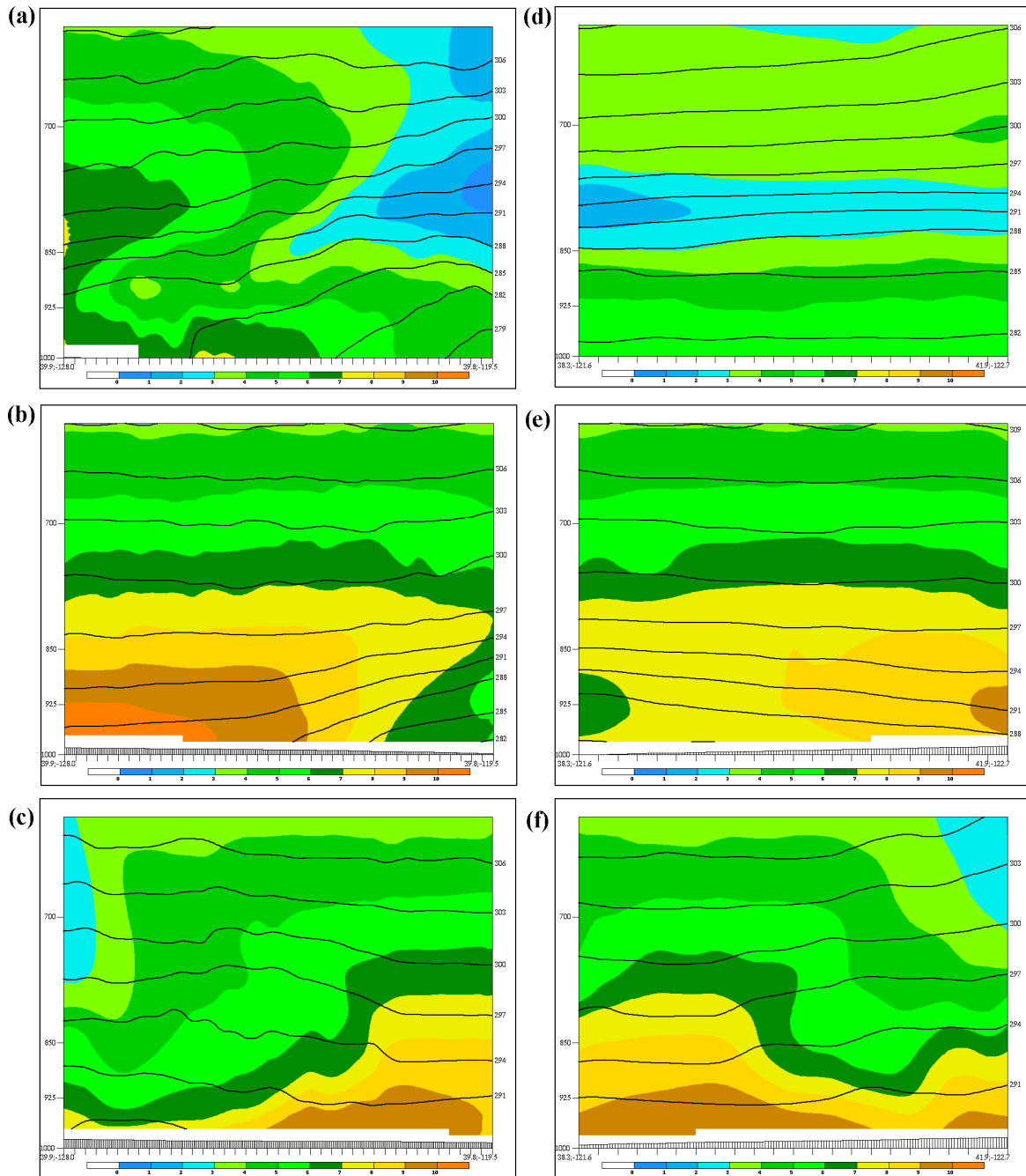


Figure 30: All figures are NOTER WRF cross-sections of potential temperature (contours in K) and water vapor mixing ratio (shaded in g kg^{-1}): for cross-section Y (see Fig. 7) (a) 00 UTC 30 Dec., (b) 12 UTC 30 Dec., and (c) 00 UTC 31 Dec., 2005; for cross-section Z (d) 12 UTC 30 Dec., (e) 00 UTC 31 Dec., and (f) 12 UTC 31 Dec.

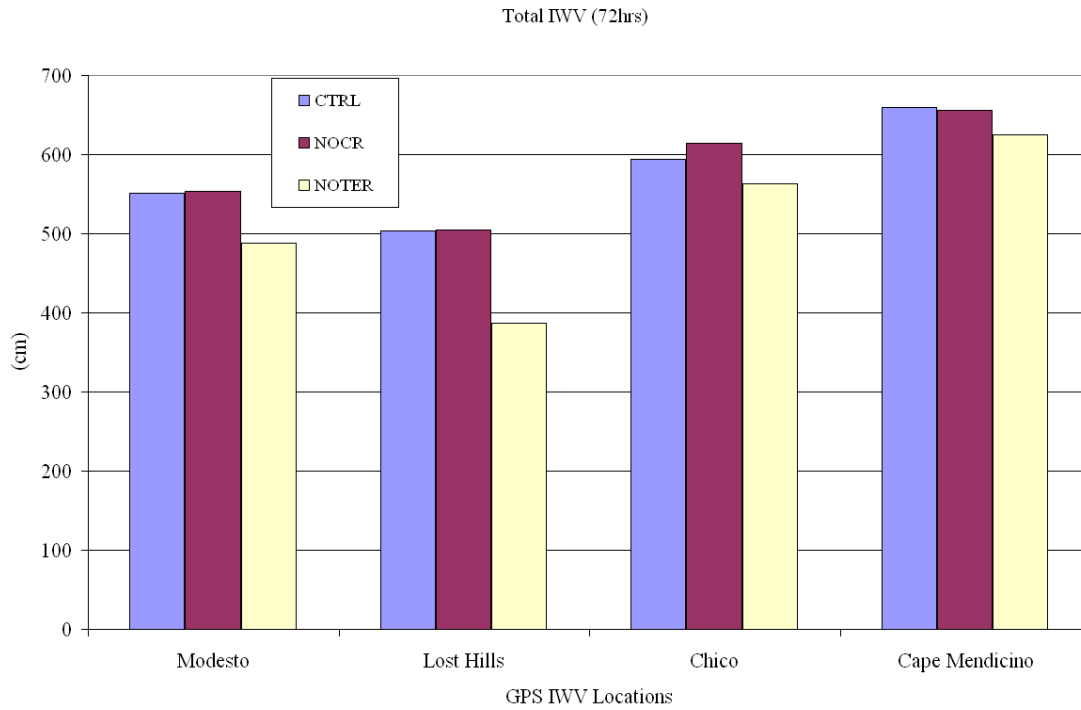


Figure 31: Total 72 hour WRF simulated IWV (in cm) at GPS location from the WRF CTRL, NOTER, and NOCR simulations.

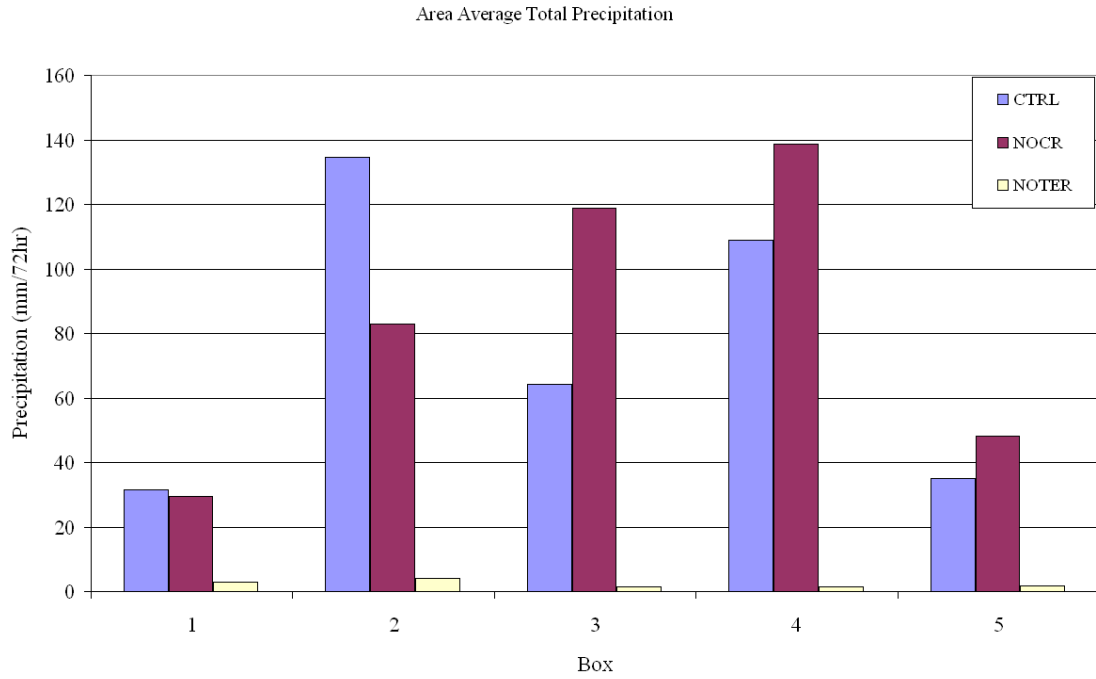


Figure 32. WRF 72 hour area average total precipitation (mm) in boxes 1-5 for the CTRL, NOTER, and NOCR simulations.

Table 1. Drying ratios from past studies for various mountain ranges; Alps (Smith et al. 2003), Andes (Smith and Evans 2007), and Oregon Cascades (Smith et al. 2005). The drying ratio for Northern California includes both the Coastal Range and Sierra Nevada range and is an average of 15 cases presented in Didlake (2007).

Mountain Range	Drying Ratio (%)
Alps	35
Andes	50
N. California	32
Oregon Cascades	43

Table 2a. Summary of drying ratios for the CTRL, NOCR, and NOTER runs for box side A and the subsequent downstream sides.

	CTRL	NOCR	NOTER
Box Side	Total Flux ($\times 10^{13}$ kg 72hr ⁻¹) through A		
A	1.58	1.58	1.37
	% reduced of Side A Flux		
B	12	7	2.6
C	36	22	2.8
D	41	36	2.9
E	55	55	3.2

Table 2b. Summary of drying ratios for the CTRL, NOCR, and NOTER runs for box side B and the subsequent downstream sides.

	CTRL	NOCR	NOTER
Box Side	Total Flux ($\times 10^{13}$ kg 72hr ⁻¹) through B		
B	1.39	1.47	1.33
	% reduced of Side B Flux		
C	28	16	0.2
D	32	30	0.3
E	49	51	0.7

Table 2c. Summary of drying ratios for the CTRL, NOCR, and NOTER runs for box side D and the subsequent downstream side.

	CTRL	NOCR	NOTER
Box Side	Total Flux ($\times 10^{13}$ kg 72hr ⁻¹) through D		
D	.94	1.02	1.34
	% reduced of Side D Flux		
E	25	30	1.1

BIBLIOGRAPHY

- Barstard, I., and R. B. Smith, 2005: Evaluation of an orographic precipitation model. *J. Hydrometeor.*, **6**, 85-99.
- Bond, N. A., C. F. Mass, B. F. Smull, R. A. Houze, Jr., M.-J. Yang, B. A. Colle, S. A. Braun, M. A. Shapiro, B. R. Colman, P. J. Neiman, J. E. Overland, W. D. Neff, and J. D. Doyle, 1997: The Coastal Observation and Simulation with Topography (COAST) experiment. *Bull. Amer. Meteor. Soc.*, **78**, 1941-1955.
- Browning, K. A., 1990: Organization of clouds and precipitation in extratropical cyclones. *Extratropical Cyclones: The Erik Palman Memorial Volume*, C. W. Newton and E. Holopainen, Eds., Amer. Meteor. Soc., 129-153.
- Bruintjes, R. T., T. L. Clark, and W. D. Hall 1994: Interactions between topographic airflow and cloud precipitation development during the passage of a winter storm in Arizona. *J. Atmos. Sci.*, **51**, 48-67.
- Buzzi A., N. Tartaglione, and P. Malguzzi, 1998: Numerical simulations of the 1994 Piedmont flood: Role of orography and moist processes. *Mon. Wea. Rev.*, **126**, 2369-2383.
- Carlson, T. N., 1980: Airflow through midlatitude cyclones and the comma cloud pattern. *Mon. Wea. Rev.*, **08**, 1498-1509.

- Colle, B. A., 2004: Sensitivity of orographic precipitation to changing ambient conditions and terrain geometries: An idealized modeling perspective. *J. Atmos. Sci.*, **61**, 588-606.
- Didlake, A. C., Jr., 2007: An analysis of water vapor flux and orographic precipitation in Northern California. B.S. Thesis, Dept. of Geology and Geophysics, Yale University, 47pp.
- Doswell, C. A., C. Ramis, R. Romero, and S. Alonso, 1998: A diagnostic study of three heavy precipitation episodes in the western Mediterranean region. *Wea. and Forecasting*, **13**, 102-124.
- Galewsky, J., and A. Sobel, 2005: Moist Dynamics and Orographic Precipitation in Northern and Central California during the New Year's Flood of 1997. *Mon. Wea. Rev.*, **133**, 1594–1612.
- Gavert, M. F., B. F. Smull, and C. F. Mass, 2007: Multiscale mountain waves influencing a major orographic precipitation event. *J. Atmos. Sci.*, **64**, 711-737.
- Heggli, M. F., and R. M. Rauber, 1988: The characteristics and evolution of super-cooled water in winter time storms over the Sierra Nevada: A summary of microwave radiometric measurements taken during the Sierra Cooperative Pilot Project. *J. Appl. Meteor.*, **27**, 989-1015.

Lackmann, G., and J. Gyakum, 1999: Heavy cold-season precipitation in the northwestern United States: Synoptic climatology and an analysis of the flood of 17–18 January 1986. *Wea. Forecasting*, **14**, 687–700.

Lackmann, G., 2002: Cold-frontal potential vorticity maxima, the low-level jet, and moisture transport in extra-tropical cyclones. *Mon. Wea. Rev.*, **130**, 59-74.

Lin, Y.-L., S.Chiao, T.-A. Wang, M. L. Kaplan, and R. Weglarz, 2001: Some common ingredients for heavy orographic precipitation. *Wea. Forecasting*, **16**, 633-660.

Mesinger, F., and coauthors, 2006: North American Regional Reanalysis. *Bull. Amer. Met. Soc.*, **87**, 343-360.

Neiman, P. J., F. M. Ralph, A. B. White, J. D. Lundquist, and M. D. Dettinger, 2007: Meteorological characteristics and overland precipitation impacts of atmospheric rivers affecting the west coast of North America based on eight years of SSM/I satellite observations. *J. Hydrometeorology*., submitted.

Parish, T. R., 1982: Barrier winds along the Sierra Nevada Mountains. *J. Appl. Metoer.*, **21**, 925-930.

Ralph, F. M., P. J. Neiman, and G. A. Wick, 2004: Satellite and CALJET aircraft observations of atmospheric rivers over the eastern North Pacific Ocean during the winter of 1997/98. *Mon. Wea. Rev.*, **132**, 1721–1745.

Ralph, F. M., P. J. Neiman, and R. Rotunno, 2005a: Dropsonde observations in low-level jets over the northeastern Pacific Ocean from CALJET-1998 and PACJET-2001: Mean vertical profile and atmospheric river characteristics. *Mon. Wea. Rev.*, **133**, 889-910.

Reeves, H. D., 2006: Dynamic forcing and mesoscale variability of heavy precipitation events over the Sierra Nevada Mountains. Ph.D. dissertation, North Carolina State University. 140 pp.

Rotunno, R. and R. Ferretti, 2001: Mechanisms of intense Alpine rainfall. *J. Atmos. Sci.*, **58**, 1732-1749.

Skamarock, W. C., J. B. Klemp, J. Dudhia, D. O. Gill, D. M. Barker, W. Wang and J. G. Powers, 2005: A Description of the Advanced Research WRF Version 2. *NCAR Tech. Note*.

Skamarock, W. C., 2006: Positive-Definite and Monotonic Limiters for Unrestricted-Timestep Transport Schemes. *Mon. Wea. Rev.*, **134**, 2241-2250.

- Skamarock, W. C., and J. B. Klemp, 2007: A time-split nonhydrostatic atmospheric model for research and NWP applications. *J. Comp. Phys.*, special issue on environmental modeling. *Accepted*.
- Smith, R. B, Q. Jiang, M. G. Fearon, P. Tabary, M. Dorninger, J. D. Doyle, and R. Beniot, 2003: Orographic precipitation and air mass transformation: An Alpine example. *Q. J. R. Met. Soc.*, **129**, 433-454.
- Smith, R. B., I. Barstard, and L. Bonneau, 2005: Orographic precipitation and Oregon's climate transition. *J. Atmos. Sci.*, **62**, 177-191.
- Smith, R. B. and J. P. Evans, 2007: Orographic precipitation and isotope fractionation over the southern Andes. *J. Hydrometeor.*, **8**, 3-19.
- Stoelinga, M. T., P. V. Hobbs, C. F. Mass, J. D. Locatelli, B. A. Colle, R. A. Houze, Jr., A. L. Rangno, N. A. Bond, B. F. Smull, R. M. Rasmussen, G. Thompson, and B. R. Colman, 2003: Improvement of Microphysical Parameterization through Observational Verification Experiment (IMPROVE). *Bull. Amer. Meteor. Soc.*, **84**, 1807-1826.
- Strangeways, I. C., 1996: Back to basics: the 'met. enclosure' : Part 2(b) -Raingauges, their errors. *Weather*, **51**, 298-303.

Wentz F. J, 1997: A well-calibrated ocean algorithm for SSM/I, *J. Geophys. Res.*, **102**, 8703-8718.

White, A. B., P. J. Neiman, R. M. Ralph, D. E. Kingsmill, and P. O. G. Persson, 2003: Coastal orographic rainfall processes observed by radar during the California Land-Falling Jets Experiment. *J. Hydrometeor.*, **4**, 264-282

Zhu, Y., and R. E. Newell, 1998: A proposed algorithm for moisture fluxes from atmospheric rivers. *Mon. Wea. Rev.*, **126**, 725-735.